J. Fluid Mech. (2010), *vol.* 665, *pp.* 120–157.
doi:10.1017/S0022112010003848

Effects of a geometrical surface disturbance on flow past a circular cylinder: a large-scale spanwise wire

A. EKMEKCI[1]† AND D. ROCKWELL[2]

[1]Institute for Aerospace Studies, University of Toronto, Ontario, Canada M3H 5T6

[2]Department of Mechanical Engineering, Lehigh University, PA 18015, USA

(Received 29 September 2009; revised 14 July 2010; accepted 14 July 2010;
first published online 26 October 2010)

Flow control induced by a single wire that is attached on the outer surface and parallel to the span of a stationary circular cylinder is investigated experimentally. The Reynolds number has a value of 10 000 and the wire diameter is nearly two orders of magnitude smaller than the cylinder diameter, while being larger than the thickness of the unperturbed boundary layer forming around the cylinder. A technique of high-image-density particle image velocimetry is used to characterize mean and unsteady structures of the separating shear layer and the near wake. Only one of the shear layers is directly perturbed by the surface wire. This disturbance, however, has important global consequences over the entire near wake, provided that the wire is located within a certain range of angular positions with respect to the approach flow. Over this range, there are two angles that can be defined as critical on the basis of the streamwise extent of the near-wake structure. In a simplified sense, these critical angles are associated with significant extension and contraction of the near wake, relative to the wake in the absence of the effect of a surface disturbance. The critical angle of the wire that yields the most significant extension of the near wake is also found to lead to bistable oscillations of the separating shear layer at irregular time intervals, much longer than the time scale associated with the classical Kármán vortex shedding. The foregoing two critical states of extension and contraction of the near wake are, respectively, linked to attenuation or enhancement of the Kármán instability. Moreover, the onset of the shear-layer instability, Reynolds stress, Strouhal number and the transverse extent of shear-layer flapping are all shown to depend on the angular position of the wire within the defined range of angles.

Key words: instability control, vortex streets, vortex shedding

1. Introduction

Vortex shedding from a cylindrical, or near cylindrical, structure gives rise to unsteady loading which, in certain cases, can lead to large-amplitude structural vibration. A wide variety of slender structures, in the areas of wind and ocean engineering, are subject to vortex-induced vibration as a potential threat to their fatigue life and integrity. Examples include risers of offshore platforms, cables and ropes used for mooring and instrumentation in the ocean, heat exchanger tubes used

† Email address for correspondence: ekmekci@utias.utoronto.ca

in nuclear power plants, cooling towers, tall buildings, industrial chimneys, aircraft control surfaces and antennas.

Alleviation of the unsteady loading of a cylindrical structure, and in certain cases, its vibration, can be achieved by application of a geometric disturbance(s), for example, helical protuberances, staggered separation wires and collars and rings, all of which are mounted on the surface of the cylinder. In addition, wires, as well as various configurations of perforated, axial-slat and axial-rod shrouds mounted away from the cylinder surface, have also been proven effective as passive suppression measures. Many of these approaches are described by Zdravkovich (1981) and Naudascher & Rockwell (2005).

The present investigation addresses alterations of the flow structure past a stationary cylinder due to a single wire mounted spanwise along its surface. Emphasis is on the quantitative features of the flow physics. In the following, previous related investigations, involving basic classes of surface disturbances, are briefly summarized, which leads to a definition of unresolved issues.

1.1. *Previous related investigations*

1.1.1. *Helical surface disturbances*

Helical surface disturbances are the most commonly employed passive control measures to suppress or at least reduce the vortex-induced vibration of cylindrical members, as reviewed by Zdravkovich (1981) and Naudascher & Rockwell (2005). Among the disadvantages of helical disturbances are: substantial increase in mean drag (Cowdrey & Lawes 1959), significant reduction of effectiveness in turbulent approach flow (Gartshore, Khanna & Laccinole 1979), and inefficiency below a critical mass-damping parameter (Ruscheweyh 1981).

Helical strakes. Investigations on the effects of helical configurations with rectangular cross-section by Scruton & Walshe (1957), Woodgate & Mabey (1959), Hirsch, Ruscheweyh & Zutt (1975), Wong & Kokkalis (1982) and Every, King & Weaver (1982) focused primarily on reduction of the amplitude of the cylinder vibration induced by Kármán vortex shedding, as summarized by Naudascher & Rockwell (2005). The effectiveness of strakes as a function of the mass-damping parameter of the elastically-mounted/elastic cylinder was assessed by Ruscheweyh (1981).

Helical wires. Surface wires of relatively small diameter, in the form of a helical pattern, can lead to significant reduction of unsteady loading and vibration of the cylinder. Nakagawa *et al.* (1959, 1963) employed a helical wire pattern within the supercritical range of Reynolds number. Even if the cylinder has a small spanwise extent, as for the configuration of a short cylindrical buoy, this type of configuration of winding can be effective. Chyu & Rockwell (2002) and Saelim (2003) characterized the flow structure in the near wake of a cylinder with a relatively large-diameter helical winding, up to the order of 10 % of the cylinder diameter. In their investigations, quantitative imaging led to patterns of velocity and vorticity.

Helical stranded cables. Helical pattern of surface disturbance is inherent to stranded cables, which are woven from a number of wires. Such cables are employed in a range of practical scenarios. Examples include underwater towing cables, mooring lines of ocean structures, overhead transmission lines and cables on suspension bridges. The early investigations of Votaw & Griffin (1971) and Horton *et al.* (1987) addressed, respectively, the Strouhal number and the vortex shedding characteristics for cable vibrations in a direction normal to the free stream. Vortex shedding characteristics from helical stranded cables were shown to be strongly influenced by the number

of strands and the yaw angle by Votaw & Griffin (1971), Horton *et al.* (1987), Batill, Nelson & Nebres (1988) and Nebres (1989). Nebres, Batill & Nelson (1993) determined the surface pressure profiles for several classes of cables, in relation to the time-averaged (steady) lift and normal drag. In addition, with the aid of smoke visualization, they characterized patterns of cells in the near wake, arising from spanwise disturbance of the stranded cable. Further, related investigations are summarized by Nebres *et al.* (1993).

Helical fluid injection. The existence of a geometrical surface disturbance can be simulated via steady or unsteady injection of fluid through helical patterns of small holes about the surface of a smooth cylinder. Lin, Towfighi & Rockwell (1995) used quantitative imaging to determine alteration of the patterns of vortex formation in the near wake through helical fluid injection. They demonstrated that even when the dimensionless injection ratio of the fluid from the surface has a relatively small magnitude, substantial alterations of the near-wake patterns are attainable. These findings suggest that geometric surface disturbances of small amplitude can effectively alter the wake.

1.1.2. *Spanwise surface disturbances*

The three-dimensionality of the helical disturbances increases the complexity of ensuing flow fields. In search of a physical understanding for flow control through surface disturbances, a number of investigators have turned their attention to cylinders with spanwise (straight) disturbances with the intention of simplifying the geometry to conduct thorough analyses. To this end, previous investigations have shown the effects of spanwise wires on the drag coefficient, surface pressure profiles and flow patterns. Fage & Warsap (1929) studied effects of two spanwise surface wires on the drag force and the circumferential pressure characteristics of a stationary cylinder in the subcritical flow regime. Their wires ranged in size from 0.03δ to 1.61δ, where δ is the boundary-layer thickness. They achieved reduction of the drag coefficient and modification of the pressure distribution for certain configurations of two spanwise wires located at $\pm 65^\circ$ from the stagnation point, even for wires having a diameter smaller than the boundary-layer thickness. They also showed that these effects are enhanced at higher Reynolds numbers, but do not vary appreciably with wire diameter, provided the wire has a size slightly larger than the boundary-layer thickness. They did not investigate the effect of the angular position of the wire, but they deduced from surface pressure measurements that small wires located at angles of $\pm 25^\circ$ with respect to the forward stagnation point have very little influence. Accordingly, they speculated that the wire-induced disturbance is greatest when it is located just upstream of the separation point. James & Truong (1972) showed, for the case of a single spanwise wire, that either a substantial increase or decrease in mean drag is attainable, depending upon both the wire diameter relative to the boundary-layer thickness and the angular position of the wire. Aiba, Ota & Tsuchida (1979) affixed two spanwise wires, having a wire to cylinder diameter ratio of $d/D = 0.0046$, at locations $\theta = \pm 65^\circ$ from the forward stagnation point on the cylinder surface. The Reynolds number ranged from $Re = 12\,000$ to $52\,000$. Their study clarified the interactions between the heat transfer and the flow. Particularly, the heat transfer from cylinder to the flow is found to be closely related to the width of the near wake. Igarashi (1986) visualized the flow patterns for a range of wire diameters and angular positions and classified the flow in terms of the onset of turbulence and separation at the wire. Three distinct regimes were deduced. The flow may: relaminarize beyond the wire; form a turbulent boundary layer immediately downstream of the wire; or

completely separate at the wire. Fujita, Takahama & Kawai (1985) studied the effects of wires attached at two symmetrical positions from the forward stagnation point of a cylinder at $Re = 50\,000$. Based on pressure distributions around the cylinder for various wire diameters and angular positions, they also classified the flow into three patterns. The first pattern involves a separation bubble behind the wire. After reattachment of the shear layer to the cylinder surface, the flow pattern becomes the same as the one observed on a bare cylinder. The second pattern also shows a separation bubble behind the wire; however, the final separation angle from the cylinder surface is larger than that of a bare cylinder. The third pattern is when flow separates at the wire with no reattachment to the cylinder surface.

More recently, Nebres (1992) and Nebres & Batill (1993) investigated the effects of a single spanwise wire. They considered variations of wire diameter, Reynolds number and angular position of the wire. Their measurements included vortex shedding frequency, spacing between the shear layers and vortices in the vortex street, as well as time-averaged distributions of the surface pressure. They showed that the shedding frequency is affected only over a certain range of angular positions of the wire. Their measurements of Strouhal number with a hot wire probe, as a function of angular position of the wire, revealed several angles at which fundamental changes occurred. One of these angles, designated as a critical angle θ_c, corresponded to an abrupt change in the shedding frequency. They also observed that, with a decrease in wire size, there is a decrease in the range of angular positions of the wire for which the Strouhal number shows a variation, as well as a reduction in the magnitude of variation of the Strouhal number. Nebres (1992) and Nebres & Batill (1993) characterized four flow regimes on the basis of time-averaged surface pressure distributions, as a function of angular position of the wire. These regimes included definition of specific angular positions of the wire, from smaller to larger angles designated as θ_t, θ_c and θ_r. They revealed the following. In the range $\theta = 0^\circ - \theta_t$, boundary-layer reattachment downstream of the wire is followed by laminar separation. In the range $\theta = \theta_t - \theta_c$, boundary-layer reattachment occurs. The separation is, however, delayed due to boundary-layer transition. In the range $\theta = \theta_c - \theta_r$, complete separation takes place at the wire. For $\theta > \theta_r$, the wire shows insignificant effect on the flow. These regimes were also supported by the smoke visualization of Nebres (1992). Nigim & Batill (1997) characterized, in a similar fashion as the foregoing, the effects of a relatively large number of equally spaced spanwise wires along the surface of the cylinder, and detected changes of the drag coefficient and the Strouhal number.

Hover & Triantafyllou (1999) investigated the effects of two small spanwise wires located at $\theta = \pm 65^\circ$, and Hover & Triantafyllou (2000) and Hover, Tvedt & Triantafyllou (2001) studied their effects at angles $\theta = \pm 70^\circ$ from the stagnation point. Their investigations, which included both stationary and oscillating cylinders, showed significant alterations of the drag and lift coefficients, as well as the Strouhal number, as a function of Reynolds number in the subcritical range.

Alam, Sakamoto & Moriya (2003) showed that the optimum angular position for reducing fluid forces acting on a cylinder is 30°, at $Re = 55\,000$, with deployment of two tripping rods of 5 mm diameter, positioned symmetrically with a gap distance of 0.4 mm from the cylinder surface. Three different flow separation–reattachment patterns were shown to exist via the use of a surface-oil film technique when the tripping rods were between 20° and 60°. These flow patterns were linked to different trends of force coefficients. One regime, from $\theta = 20^\circ$ to 40°, involves reattachment of the separating boundary layer after the tripping rods. Another regime, from $\theta = 45^\circ$ to 60°, involves separation at the tripping rods such that the rods force the separated

layer to deflect outwards. The third regime, from $\theta = 41^\circ$ to 44°, involves bistable flow in which the two flow patterns intermittently appear.

1.2. *Unresolved issues*

The investigations described in the foregoing have considerably advanced our understanding of several aspects related to flow past a cylinder with surface disturbances. Taken together, they lead to the following unexplored issues for further consideration.

(i) Extensive investigation of induced structural loading, shedding frequency, surface pressure distribution and qualitative visualization of the near-wake patterns in previous related research has provided valuable insight. A further physical basis for interpretation of the control of flow past a cylinder via surface disturbances can be provided by wholefield quantitative characterization of the flow structure, involving both time-averaged and instantaneous representations. Pointwise frequency measurements of velocity fluctuations in the flow have been established previously, however global spectral analyses over the entire near-wake and shear-layer separation regions have remained unexplored. Particularly important is the possibility of either attenuation or enhancement of the classical Kármán vortex shedding, at a sufficiently high Reynolds number, where small-scale vortices exist in the separating shear layer.

(ii) It is recognized, on the basis of pointwise measurements, that the predominant frequency of Kármán vortex shedding can undergo significant changes when the angular position of a spanwise surface wire is varied. This approach has led to the definition of critical states, in terms of the Strouhal number of vortex formation. It would be insightful to seek and define critical states based on global quantitative patterns of the near-wake structure.

(iii) Insight into the behaviour of the wire-induced separation/reattachment process, as well as the effect of the wire on the onset of the shear-layer instability, can be gained by quantitative imaging of the flow patterns.

(iv) For passive control techniques that influence only one of the separating shear layers from the cylinder, as is the case in the present investigation, the issue arises as to what extent the modified layer exerts a global influence over the entire near wake, which, of course, is formed from two separating shear layers.

The foregoing issues will be addressed using a cinema technique of high-image-density particle image velocimetry (PIV), which will provide quantitative interpretation of the unresolved flow physics induced by a single spanwise wire that is two orders of magnitude smaller than the cylinder diameter.

2. Experimental system and techniques

Experiments were conducted at Lehigh University in a recirculating-type free-surface water channel, providing continuous flow in the horizontal direction. The main test section of this channel was made of transparent Plexiglas material, in order to allow optical access to the flow, and had a length of 5435 mm, a width of 613 mm and a depth of 594 mm. Upstream of the test section, the flow passed through a settling chamber with a flow conditioning unit composed of a set of honeycomb and screens, and then through a 3:1 contraction. This arrangement yielded free-stream turbulence intensity less than 0.1 %. Additional characteristics of this facility are described in Ekmekci (2006).

The cylinder, used in the present investigation, had a diameter $D = 50.8$ mm, based on which the free-stream velocity of $U_o = 197\,\mathrm{mm\,s^{-1}}$ corresponds to a Reynolds

number of $Re = 10\,000$. This subcritical value of Reynolds number was employed in all the experiments. A wire, made of nylon fishing line, was glued on the surface of the cylinder parallel to its longitudinal axis. The diameter of this wire was $d = 1.48$ mm, giving a ratio of wire to cylinder diameter $d/D = 0.029$. During the course of the investigation, different angular positions θ of this spanwise wire, relative to the approach flow, were addressed. To this end, the value of θ was varied by rotating the entire cylinder–wire model around the longitudinal axis of the cylinder in 5° increments.

Based on the work of Nebres (1992), the normalized value of the boundary-layer thickness δ/D around a smooth cylinder, i.e. a cylinder with no surface perturbation, at $Re = 10\,000$ varies from $\delta/D = 0.015$ to 0.020 between the angular locations $\theta = 5°$ to 70°, referenced from the forward stagnation point. The diameter ratio $d/D = 0.029$ of the surface wire, employed in this investigation, is larger than these values of δ/D. Hence, on the basis of the comparison with the unperturbed boundary-layer thickness, the wire under consideration can be referred to as a large-scale wire.

In the experiments, the cylinder–wire system was mounted rigidly with a vertical orientation inside the water channel, equidistant from the channel sidewalls. At the top, it was bounded by the water–air type free surface and at the bottom, by a special end plate arrangement. This end plate was placed at an elevation of $1D$ from the channel floor with the purpose of isolating the flow past the bottom end of the cylinder from the turbulent boundary layer forming along the channel floor. The water height above the end plate provided an effective aspect ratio of $L/D = 8.78$. The end plate was rectangular in shape. In order not to disturb the inflow conditions, it was bevelled on the bottom side of its leading edge with an angle of 23.6° and was flat on the top. Its streamwise length of $7.5D$ spanned the entire width of the channel. This end plate design promoted quasi-two-dimensional flow conditions as shown in Ekmekci (2006) and Dong *et al.* (2006), where the degree of spanwise two-dimensionality, based on quantitative imaging, is described in terms of a sharply defined spanwise demarcation line, located at the interface of positive and negative contours of constant streamwise velocity. Therein, the root-mean-square (r.m.s.) deviation of the distance of this demarcation line from the base of the cylinder was found to be 2.6 % of its average distance.

A technique of high-image-density PIV was employed for the quantitative imaging of the flow. For successive measurement of instantaneous velocity fields, the flow was illuminated with short-duration laser-sheet pulses of 1 mm thickness at the planar flow region of interest. A double-pulsed Nd:YAG laser system, operating at 120 mJ per pulse, was used for the sequential generation of the laser pulses. The fluid motion in the illuminated region was made visible by seeding the flow with neutrally-buoyant tracer particles that are 14 μm in diameter. The images of these particles were captured via a CCD camera, having a resolution of 1008×1018 light-sensitive pixels.

The shaded areas in the schematic of figure 1 indicate the two distinct flow fields of visualization employed for imaging. Located at an elevation of three cylinder diameters from the bottom end of the cylinder, they provide complementary interpretations of the wire-induced effects on the flow structure. The larger area, designated as I in the schematic of figure 1, encompasses the near wake including the downstream region of both shear layers that separate from the smooth and wire sides of the cylinder, while the smaller area, indicated as II in figure 1, focuses on the upstream region of the shear layer that separates from the wire side of the cylinder. The effective grid region covered an area of $1.90D \times 1.83D$ with a spatial grid resolution of $0.04D$ for the field of view I, and an area of $1.19D \times 0.88D$ with a spatial resolution of $0.02D$ for

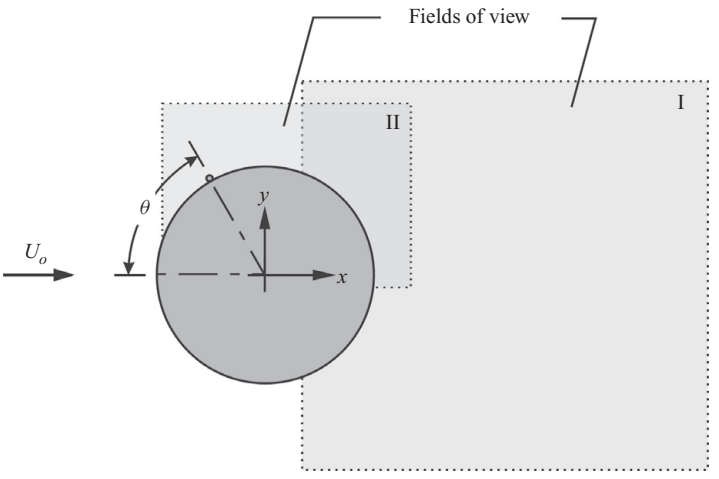

FIGURE 1. Schematic of the cylinder–wire system and the physical fields of view of visualization.

the field of view II. A frame-to-frame cross-correlation scheme with an interrogation window of 32×32 pixels with 50 % overlap generated instantaneous vector fields with a total of 2400 velocity vectors over the grid region of the field of view I and 2255 velocity vectors over the grid region of the field of view II. These instantaneous velocity fields were then used to calculate other unsteady and time-averaged flow characteristics, including vorticity, Reynolds stress correlation, streamline topology, etc. Further understanding of the flow physics, in the present investigation, was pursued by performing spectral analysis of the velocity fluctuations. Through a continuous PIV record of 13.3 s duration, a sequence of 200 image pairs was acquired at a rate of 15 frame pairs s^{-1}. To determine the time-averaged representations and the spectra, three separate data sequences were ensemble averaged, corresponding to a total of 600 snapshots of the flow. For the evaluation of the flow statistics, this approach was shown to yield experimental results in good agreement with DNS simulations by Dong *et al.* (2006).

3. Near-wake structure

In this section, the focus is on the near-wake region of the cylinder, that is, the field of view I in figure 1. First, we describe the effects of the spanwise wire on the time-averaged structure of the near wake as a function of the angular position of the wire on the cylinder surface. Using these time-averaged global patterns, we define critical states of the flow. Then, we address the unsteady characteristics of the near wake to further elaborate on the influence of the wire.

3.1. *Time-averaged patterns of the near-wake structure*

3.1.1. *Time-averaged vorticity*

Figure 2 shows the structure of the near wake in terms of time-averaged vorticity $|\langle\omega\rangle|D/U_o$ for different angular positions of the surface wire over the range $\theta = 40°$–$120°$, where the angle θ of the wire is measured relative to the forward stagnation point of the cylinder. For ease of comparison, the same contour levels of $|\langle\omega\rangle|D/U_o$ are employed for all wire positions, as defined in the figure caption. In each image of figure 2, the upper half of the cylinder corresponds to the side, where the spanwise

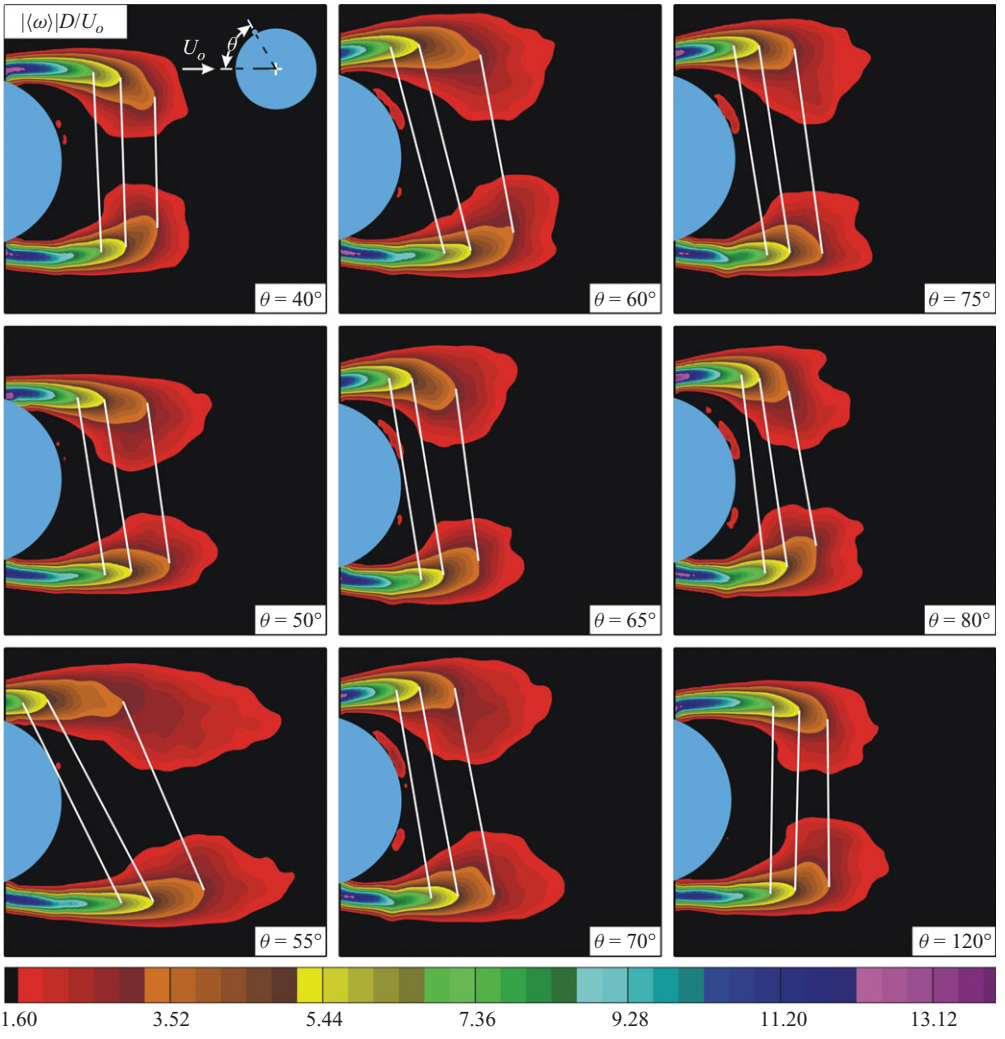

FIGURE 2. Patterns of normalized time-averaged vorticity $|\langle\omega\rangle|D/U_o$ contours for angular positions of the wire from $\theta = 40°$ to 120°. To evaluate the degree of symmetry of the shear layers, absolute values of vorticity are plotted. Minimum and incremental values are as follows: $[|\langle\omega\rangle|D/U_o]_{min} = 1.6$ and $\Delta[|\langle\omega\rangle|D/U_o] = 0.32$.

wire is located at the specified angle θ, as depicted with a sketch in the inset of the upper left image. Therefore, we will refer to the upper half of the cylinder in images as the wire side and the bottom half as the smooth side of the cylinder. In order to allow direct comparison between the wire-side and the smooth-side shear layers, absolute values of vorticity levels are presented in the contour plots of figure 2.

White lines connect the same magnitudes of vorticity levels between the opposite sides of the near wake; the angle of inclination of these lines from their upright position is an indicator of the degree to which the wire induces distortion on the near wake. At $\theta = 40°$, these reference lines show no detectable wake distortion. At $\theta = 50°$, however, inclination of all three reference lines is clearly detectable, and at $\theta = 55°$, the angle of inclination becomes relatively large. At larger values of θ, from $\theta = 60°$ to 80°, the inclination of the lines gradually decreases. Finally, at $\theta = 120°$, the reference lines

become vertical, showing no wake distortion, and resemble those at $\theta = 40°$. From the foregoing trend, it is clear that the spanwise wire has relatively little influence on the near-wake structure both at $\theta = 40°$ and 120°. However, significant asymmetry in the near wake is induced by the wire when its angular position θ lies between these values. Moreover, this asymmetry gains a maximum level at $\theta = 55°$. Also, it is clear that the inclination of the reference lines is in the same direction for all those angular positions of the wire that result in a detectable distortion in the near wake. That is, the streamwise locations of the ends of the reference lines on the wire side of the near wake are always advanced further upstream relative to the smooth side. This is an indication of a relatively early decay of time-averaged vorticity in the wire-side shear layer; the underlying reasons of this will be addressed in subsequent sections.

A further aspect involves the distance between the base of the cylinder and the downstream end of the lowest level of vorticity in both of the separating shear layers. This distance shows a distinct variation with θ. At $\theta = 55°$, it is relatively large, and at $\theta = 65°$, it is relatively short, in comparison with other angles. Viewing all the images of figure 2 as a whole, it is remarkable that, as the angular position θ of the wire increases starting from $\theta = 40°$, the streamwise extent of the near wake undergoes an extension, followed by a contraction, then relaxation towards the structure corresponding to the lack of influence of the wire. Based on this trend, we can define the angular positions of the wire that result in the largest extension and the largest contraction of the near wake, i.e. $\theta = 55°$ and 65°, as the critical angles of the wire; henceforth they will be denoted as θ_{c1} and θ_{c2}, respectively.

3.1.2. *Time-averaged streamline topology*

Corresponding plots of time-averaged streamline topology $\langle \Psi \rangle$ are given in figure 3. All patterns of $\langle \Psi \rangle$ clearly show focal points F_1 and F_2, which correspond to the apparent centres of the swirl patterns of streamlines. Also evident is a saddle point S, which represents the location of intersection of streamlines; it occurs at the closure of the near-wake bubble, which bounds the patterns of swirl streamlines. The degree of near-wake extension or contraction due to the spanwise surface wire can be defined on the basis of the patterns of $\langle \Psi \rangle$ using two types of indicators. The first involves the average of the distances of the focal points F_1 and F_2 from the base of the cylinder, and the second involves the distance of the saddle point S from the base of the cylinder. Substantial variations of both quantities clearly show the trend of extension and contraction of the near wake at the critical angles $\theta_{c1} = 55°$ and $\theta_{c2} = 65°$, respectively, in accord with the corresponding displacements of the lowest level vorticity contours shown in figure 2.

A point of further interest for each θ at which the effect of the wire is significant is that the streamwise location of the focal point F_1 in the upper part of the near wake is displaced further upstream relative to F_2 in the lower part, irrespective of whether extension or contraction of the near wake is induced. In fact, the lines connecting these focal points incline in the same direction as the reference lines on the corresponding patterns of vorticity $|\langle \omega \rangle| D/U_o$ given in figure 2. This observation in the time-averaged patterns suggests a relatively early development of the shear layer separating from the wire side of the cylinder compared to that separating from the smooth side.

3.1.3. *Time-averaged velocity fluctuations and Reynolds stress*

Figure 4 shows corresponding contour plots of the r.m.s. value of the transverse velocity fluctuation v_{rms}/U_o. An overall comparison of the colour-coded contours reveals significant variation in the peak magnitude of v_{rms}/U_o with θ. From $\theta = 40°$

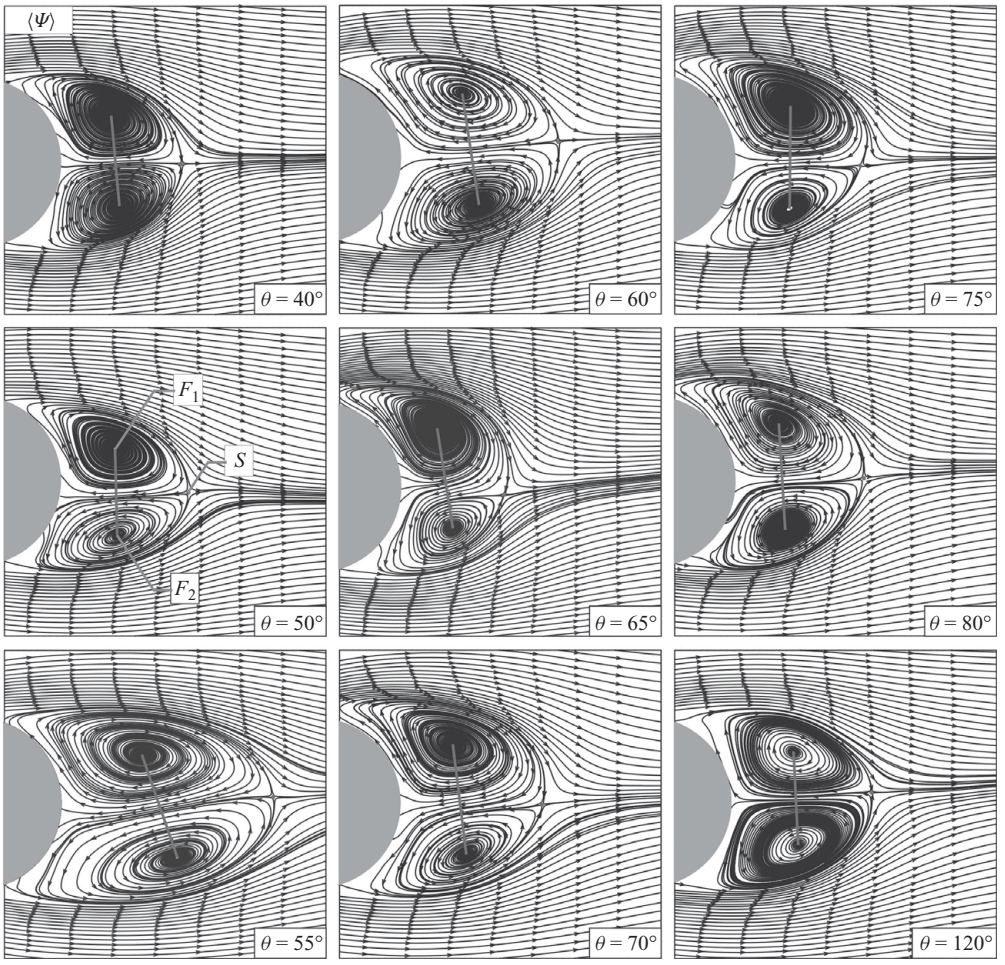

FIGURE 3. Patterns of time-averaged streamline $\langle \Psi \rangle$ topology for angular positions of the wire ranging from $\theta = 40^\circ$ to 120°. F_1 and F_2 show focal points, and S shows the saddle point. These features are only labelled on the second row left-hand side image.

to 55°, the peak value progressively decreases. In contrast, from $\theta = 55^\circ$ to 65°, it gradually increases. In fact, at $\theta_{c1} = 55^\circ$, which has been determined in figures 2 and 3 as the critical angle of the wire that results in the most significant extension of the near wake, the peak of v_{rms}/U_o attains the lowest value. In addition, at this critical angle, the streamwise location of the peak is displaced a considerable distance in the downstream direction. That is, the distance of the peak from the base of the cylinder is 55 % longer than that at $\theta = 120^\circ$, which represents a reference case with no detectable influence of the wire. On the other hand, at $\theta_{c2} = 65^\circ$, which has been found in the foregoing figures to be the critical angle of the wire that leads to significant contraction of the near wake in the streamwise direction, the peak value of v_{rms}/U_o exceeds that at the other angles and the streamwise location of this peak is relatively advanced further upstream towards the base of the cylinder.

Another pronounced effect is that the lower level contours of v_{rms}/U_o at $\theta_{c1} = 55^\circ$ exhibit strong asymmetry with respect to the plane of symmetry of the wake; significant values extend well upstream of the cylinder base along the upper shear layer

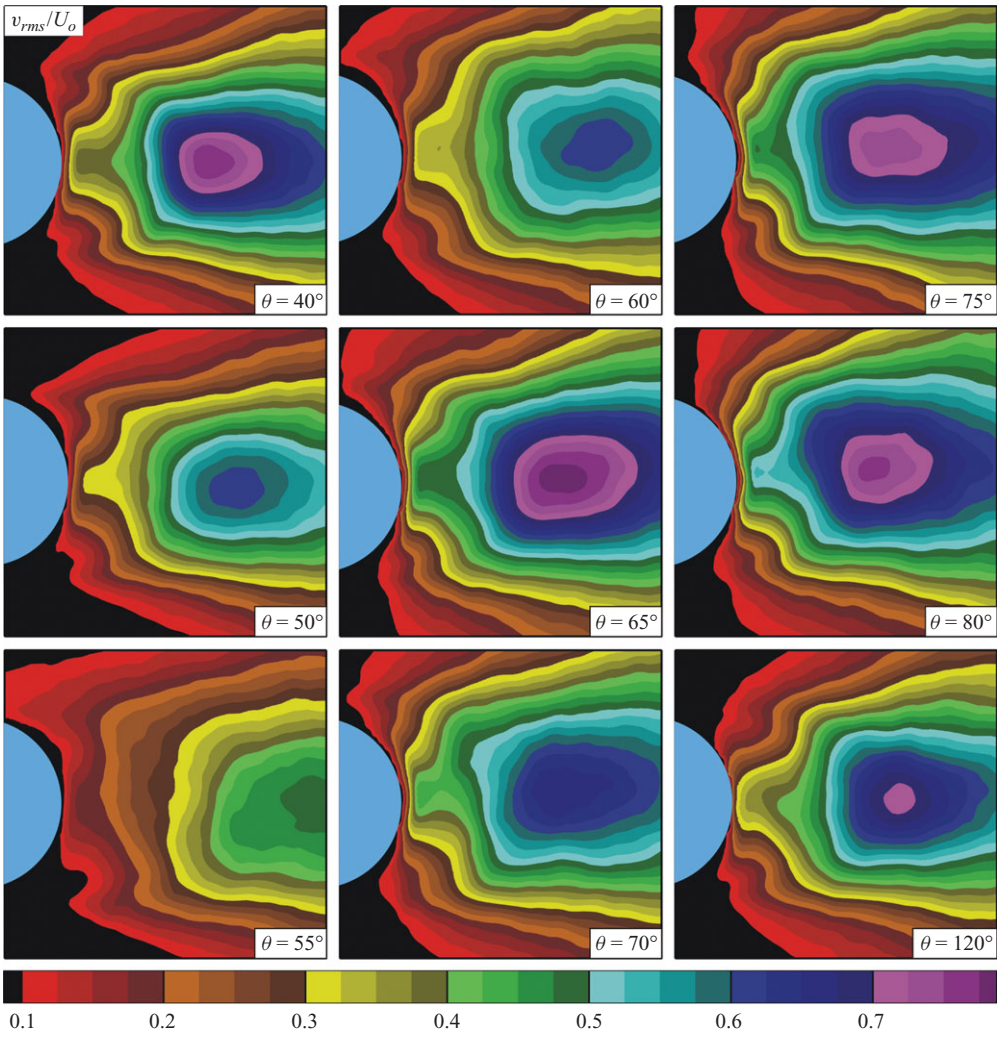

FIGURE 4. Patterns of r.m.s. of the transverse velocity for angular positions of the wire ranging from $\theta = 40°$ to 120°. Minimum and incremental values are as follows: $[v_{rms}/U_o]_{min} = 0.1$ and $\Delta[v_{rms}/U_o] = 0.025$.

towards the wire. Apparently, the presence of the wire increases the unsteadiness in the wire-side shear layer. In addition to this observation at $\theta_{c1} = 55°$, at other angular positions from $\theta = 50°$ to 80°, the patterns of v_{rms}/U_o still exhibit a discernible asymmetry. However, the upstream reach of the lower levels of v_{rms}/U_o gradually decreases as the wire location moves away from the critical angle $\theta_{c1} = 55°$. Finally, at $\theta = 40°$ and 120°, no detectable asymmetry in the levels of v_{rms}/U_o is evident; again, this observation confirms that the wire positioned at these particular angles has relatively little influence on the near-wake structure.

Figure 5 provides corresponding time-averaged contour plots of constant Reynolds stress correlation $|\langle u'v'\rangle|/U_o^2$. Herein, the absolute values of Reynolds stress are shown in order to allow direct comparison of the Reynolds stress clusters between the upper and lower parts of the near wake. Similar to the foregoing layout of v_{rms}/U_o, given in figure 4, the peak magnitudes of $|\langle u'v'\rangle|/U_o^2$ vary over the range of θ. As can be

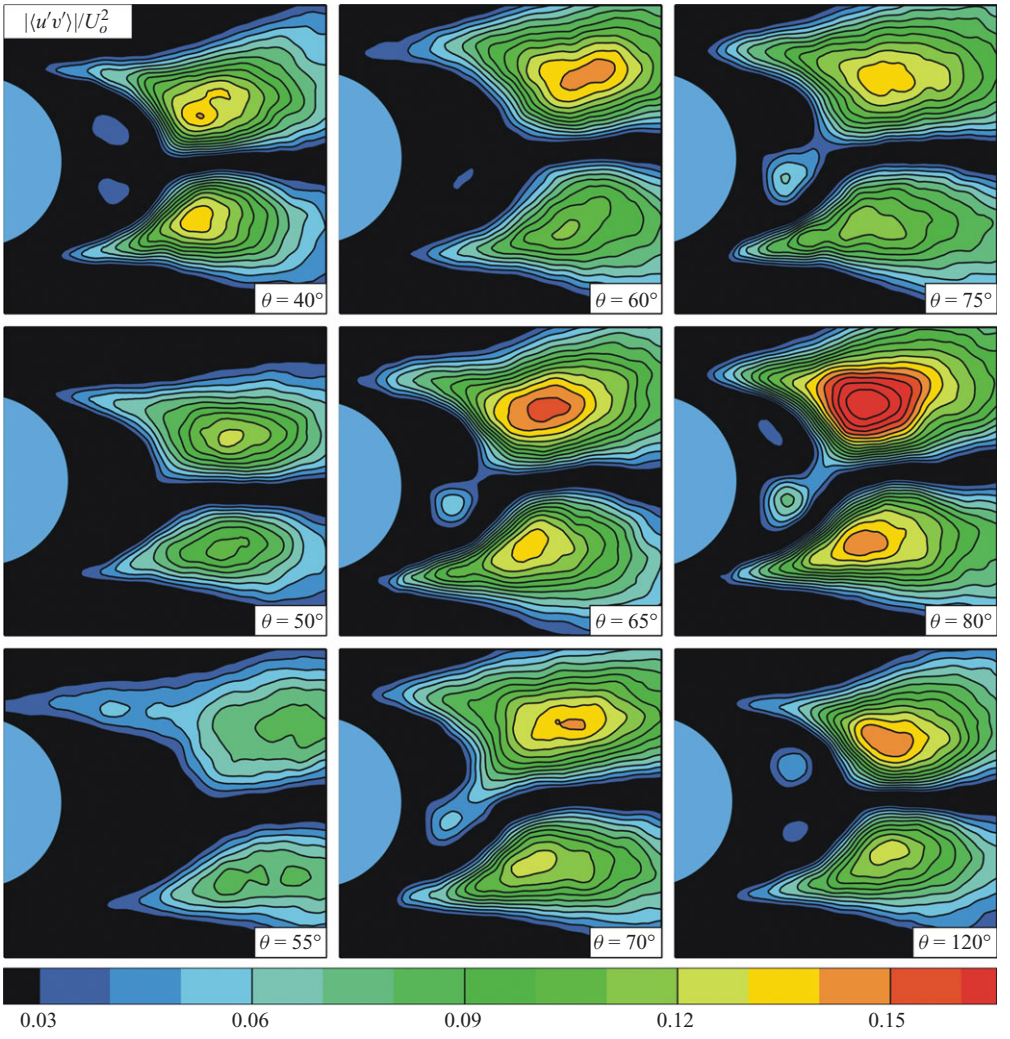

FIGURE 5. Patterns of time-averaged Reynolds stress contours for angular positions of the wire ranging from $\theta = 40°$ to 120°. For comparison of the anti-symmetric clusters of both shear layers, absolute values of the Reynolds stress levels are plotted. Minimum and incremental values are as follows: $[|\langle u'v'\rangle|/U_o^2]_{min} = 0.03$ and $\Delta[|\langle u'v'\rangle|/U_o^2] = 0.01$.

interpreted from the colour coding of the contours, from $\theta = 40°$ to 55°, the peak levels gradually decrease; in contrast, from $\theta = 55°$ to 65°, they gradually increase. Particularly for the case of the maximum near-wake extension, that is, at $\theta_{c1} = 55°$, the peak values of $|\langle u'v'\rangle|/U_o^2$ in both clusters are notably reduced, relative to the values at the other angular positions of the wire. In addition, this reduction at $\theta_{c1} = 55°$ is accompanied by an upstream reach of the low levels of $|\langle u'v'\rangle|/U_o^2$ along the upper shear layer towards the wire. Viewing the layout of figure 5 as a whole, it is apparent that as θ moves away from the critical angle $\theta_{c1} = 55°$, the degree to which low levels of $|\langle u'v'\rangle|/U_o^2$ extend along the upper shear layer gradually decreases. Regarding the second critical angle $\theta_{c2} = 65°$, which is found in the foregoing to be the critical angle of the wire at which substantial contraction of the near wake occurs, the peak values of Reynolds stress $|\langle u'v'\rangle|/U_o^2$ are perceptibly increased. For the angular positions

$\theta \geqslant 70^\circ$ in figure 5, the peak levels of $|\langle u'v' \rangle|/U_o^2$ are of the order of those of the case of $\theta = 120^\circ$, which corresponds to the wake structure that is not significantly influenced by the surface wire. One exception is detected at $\theta = 80^\circ$, that is, the peak value in the upper shear layer is relatively large. This abnormality can be attributed to the possibility that $\theta = 80^\circ$ might be a limiting (critical) angular position at which the wire still has a significant influence on the near-wake structure while being at a position after which the effect of the wire would start to become insignificant. This prospect will be further addressed subsequently.

As emphasized by Williamson (1996) in his extensive review on cylinder wakes, previous studies have generally shown that extension of the near wake in the downstream direction is associated with a decrease in the peak values of velocity fluctuation v_{rms}/U_o and Reynolds stress $\langle u'v' \rangle/U_o^2$. This concept is consistent with what we observe in relation to the extension of the near wake: at $\theta_{c1} = 55^\circ$, the peak levels of v_{rms}/U_o and $|\langle u'v' \rangle/U_o^2|$ show significant reduction in figures 4 and 5.

Up to this point, emphasis has been on the time-averaged features of the near wake of the cylinder–wire configuration. Two critical angular positions of the wire have been distinctively identified: $\theta_{c1} = 55^\circ$ and $\theta_{c2} = 65^\circ$. At these angles, the major overall changes are, respectively, significant extension and contraction of the near wake. These changes are accompanied by a degree of asymmetry of the time-averaged near-wake characteristics and an alteration in the peak values of velocity fluctuation and Reynolds stress. Furthermore, $\theta = 80^\circ$ is also hypothesized to be a third critical angle after which the effect of the wire on the near wake diminishes. In the following section, attention is directed towards the unsteady characteristics of the near wake in order to gain a deeper understanding of the flow physics.

3.2. *Unsteady structure of the near wake*

3.2.1. *Single-point spectra*

In figure 6, plots of autospectral density $S_u(f)$ of the streamwise velocity u component are shown at a number of points for the two critical angles $\theta_{c1} = 55^\circ$ and $\theta_{c2} = 65^\circ$, and for the case of $\theta = 120^\circ$. Given that the influence of the wire on the near wake is insignificant at $\theta = 120^\circ$, the latter is used as the reference case for comparison. The starting points of the arrows on the patterns of time-averaged vorticity $|\langle \omega \rangle| D/U_o$ indicate the locations of the spectra that are displayed in figure 6.

The plots at the bottom centre of figure 6 correspond to $\theta = 120^\circ$. As expected from this reference case, the spectra $S_u(f)$ clearly show a narrow-band pronounced peak at the Kármán vortex shedding frequency, which is designated as f_K.

The spectral plots for the critical angle $\theta_{c1} = 55^\circ$ are represented at the top left of figure 6. For this case, at locations close to the region of separation in the upper (wire-side) shear layer, the spectra distinctly manifest two unexpected features. First, a broad spectral peak with a low value of centre frequency f_L is dominant. This low frequency f_L is one order of magnitude smaller than the characteristic value of Kármán frequency f_K. For clarity, both f_L and f_K are marked on the top left spectral plot. Second, the spectral amplitude of the Kármán frequency f_K component is markedly attenuated; this attenuation can be clearly recognized from a comparison of the spectral amplitude of f_K with that of the reference case at $\theta = 120^\circ$. Moreover, at $\theta_{c1} = 55^\circ$, another interesting feature which occurs along the upper shear layer is that with increasing distance from the location of separation, the spectral amplitude of the low frequency f_L gradually decreases while the amplitude of the Kármán frequency f_K shows a slight increase. Notwithstanding this small rise, however, even in the downstream regions of the near wake, the amplitude of the Kármán frequency

https://doi.org/10.1017/S0022112010003848 Published online by Cambridge University Press

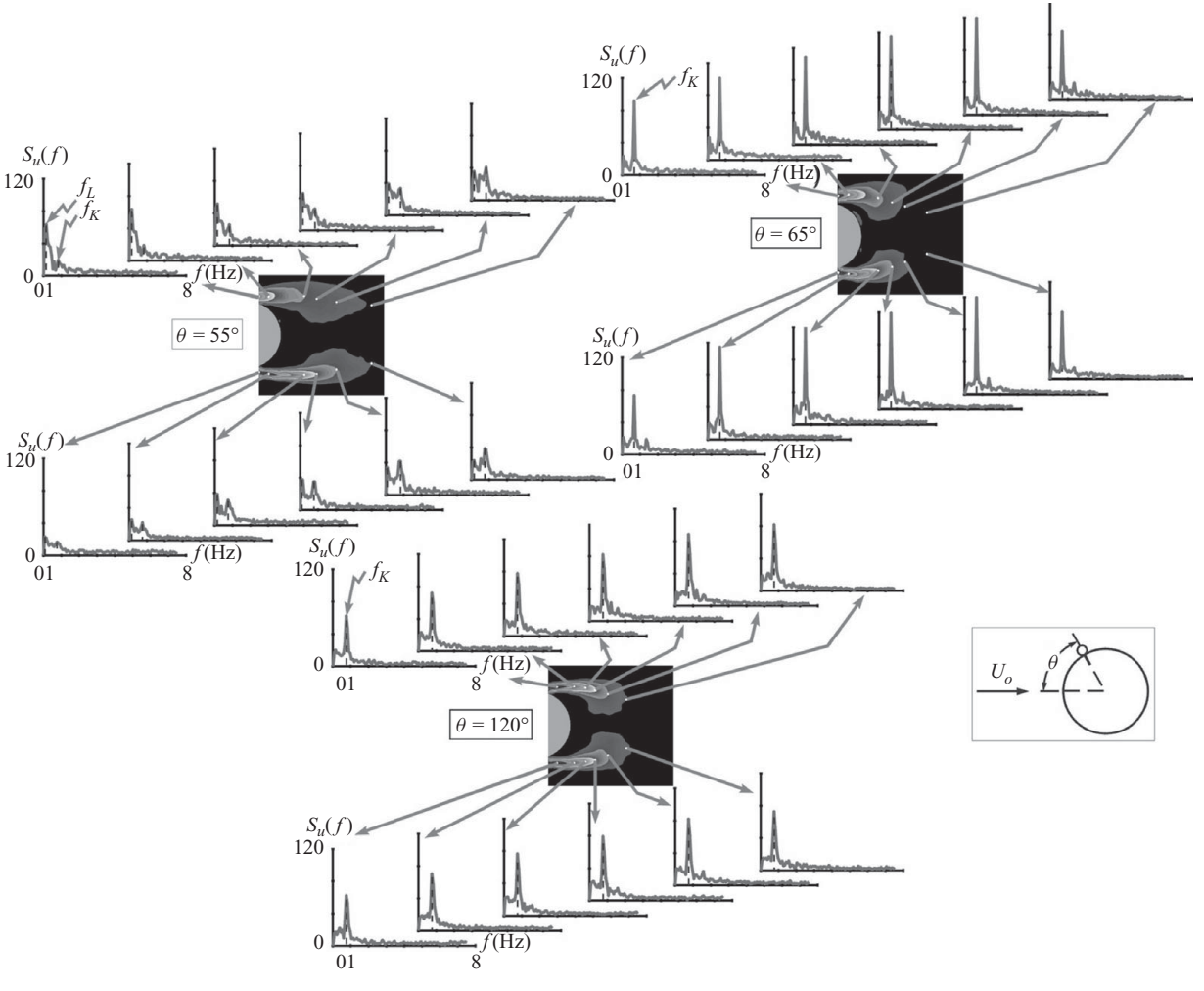

FIGURE 6. Autospectral density $S_u(f)$ of the streamwise velocity component over several points in the near wake for the surface wire locations of $\theta = 55°$, $65°$ and $120°$. On the time-averaged vorticity patterns belonging to each particular angle, the locations, where autospectra evaluations take place, are shown.

f_K remains significantly attenuated relative to that at the reference case of $\theta = 120°$. In the lower shear layer, which separates from the smooth side of the cylinder, the aforementioned peak at the low frequency f_L is also detectable at certain locations; its amplitude, however, is significantly smaller relative to the amplitude of f_L in the upstream of the upper (wire-side) shear layer. Apparently, the pronounced low-frequency fluctuations in the upstream region of the wire-side (upper) shear layer exert an influence on the smooth-side (lower) shear layer. A certain degree of such a cross-communication is indeed expected between the two shear layers. This concept of cross-communication includes not only the low-frequency fluctuations but also the fluctuations at the Kármán frequency. That is, the spectral amplitude at the Kármán frequency is remarkably attenuated, also in the smooth-side shear layer, apparent from comparison with the reference case at $\theta = 120°$. Consequently, this implies that, at $\theta_{c1} = 55°$, the single surface wire on only one side of the cylinder affects the shear layers separating from both sides and attenuates the Kármán instability in the entire near-wake region.

In the layout of figure 6, the set of spectra $S_u(f)$ at the top right corresponds to the case, where the wire is located at the second critical angle $\theta_{c2} = 65°$. The aforementioned low-frequency peak does not exist in these spectra. Moreover, comparison of the spectra at $\theta_{c2} = 65°$ with those at the reference case of $\theta = 120°$ clearly reveals that the spectral peak at the Kármán frequency f_K is notably larger in amplitude for the critical angle $\theta_{c2} = 65°$ both in the wire- and smooth-side shear layers. This observation implies that, at this particular angle, relatively pronounced Kármán vortex shedding occurs. Only one of the shear layers is directly perturbed by the wire at $\theta_{c2} = 65°$; however, here we observe again that the consequence is global.

Up to this point, we have seen that the wire at $\theta_{c1} = 55°$ induces low-frequency velocity fluctuations of broad spectral nature in the upstream region of the wire-side shear layer. Moreover, the fluctuations associated with the Kármán instability are inhibited at $\theta_{c1} = 55°$, in contrast to the effect of the wire at $\theta_{c2} = 65°$, which is found to intensify the fluctuations related to the Kármán instability. The physics of these findings at the critical angles, and the underlying phenomenon behind the low-frequency fluctuations, will be addressed in § 4, where we focus on the structure of the wire-side shear layer in the separation region. Prior to doing so, in what follows, the wire-induced unsteady characteristics over the entire region of the near wake are characterized in further detail.

3.2.2. *Strouhal number*

A detailed assessment of spectral analyses, involving thousands of points (spatial locations) over the global near-wake region, reveals a variation in the predominant frequency of velocity fluctuations from one wire position θ to another. Figure 7 indicates this variation in terms of the change of the Strouhal number $S = f_i D/U_o$, where the frequency f_i corresponds to the predominant frequency of the autospectrum $S_u(f)$ of the streamwise velocity. The uncertainty of the values of Strouhal number S is within ± 0.01. According to the plot of figure 7, there are four values of Strouhal number, one of which prevails depending on the angular position θ of the wire. Three of these values correspond to the Kármán vortex shedding frequency f_K, and are designated, from the smaller value to the larger, as S_{K1}, S_{K2} and S_{K3}; and the fourth one is a low nominal value of Strouhal number S_L corresponding to the aforementioned low frequency f_L. The latter is especially predominant in the wire side of the near wake as will be elaborated in the next section. The plot in figure 7 shows that, at $\theta = 40°$ and 50°, the Strouhal number S takes on the relatively large

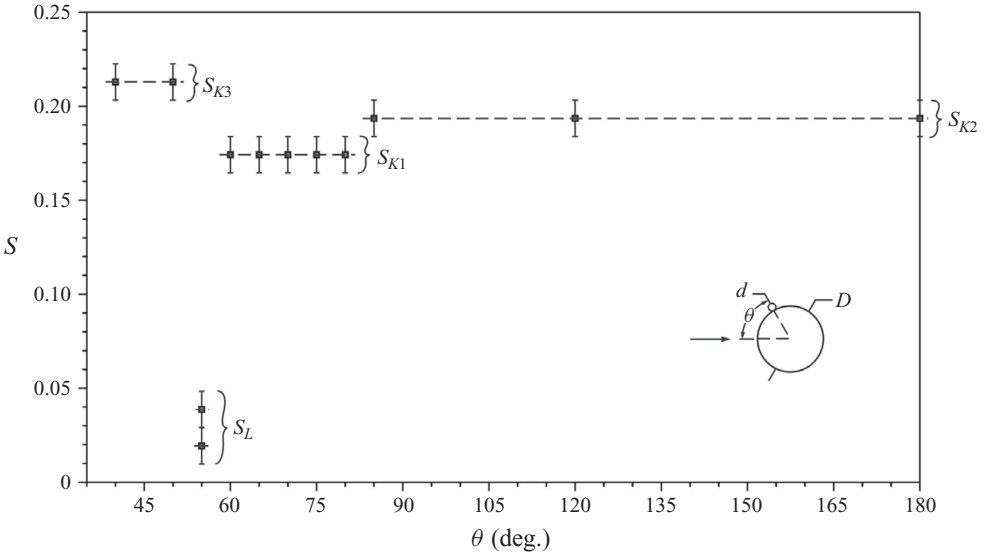

FIGURE 7. Variation of the Strouhal number S with the angular position of the wire. Herein, S corresponds to the predominant frequency of the autospectrum of streamwise velocity fluctuations in dimensionless form. The uncertainty of S is within ± 0.01.

value of S_{K3}. At $\theta_{c1} = 55°$, it abruptly drops to S_L, which is an order of magnitude smaller than the S values associated with the Kármán instability. Subsequently, at $\theta = 60°$, the value of S increases about an order of magnitude to S_{K1}. From $\theta = 60°$ to 80°, this value of S_{K1} dominates. After $\theta = 80°$, S takes on the higher value S_{K2}, and remains at that value for larger angular positions of the wire; this observation suggests that for $\theta > 80°$, the wire has no influence on the Strouhal number. This observation is in accord with the interpretations of Reynolds stress $|\langle u'v' \rangle / U_o^2|$, given in figure 5, which suggest that $\theta = 80°$ is also another critical angle.

The pioneering work of Nebres (1992) and Nebres & Batill (1993) reported the dependence of the predominant vortex shedding frequency on the angular position θ of a single spanwise wire mounted along the surface of a cylinder. Their measurements of frequency were performed in a wind tunnel, employing a hot wire probe at a single point located at the lateral position of $1.64D$ from the cylinder axis. Their investigation included a range of wire diameters and Reynolds numbers. Among all the experiments, their values of $d/D = 0.04$ and $Re = 10\,000$ are closest to the values employed in the present study, i.e. $d/D = 0.029$ and $Re = 10\,000$. For these parameters, their measurements indicate that, over a certain range of θ, the Strouhal number S shows a crater-like variation, characterized by a decrease of S, followed by an increase, as angle θ increases. In the present investigation, the variation of S, given in figure 7, follows a similar trend; yet it is not gradual, as in the findings of Nebres (1992) and Nebres & Batill (1993), owing to the relatively coarse frequency resolution of the present PIV analyses compared to the fine resolution achieved by their hot wire measurements. Quantitative comparison of the Strouhal number S obtained for $d/D = 0.04$ at $Re = 10\,000$ in the investigation of Nebres & Batill (1993) and for $d/D = 0.029$ at $Re = 10\,000$ in the present investigation also show similar values. For example, at $\theta = 40°$, 65° and 120°, the values of Nebres & Batill (1993) are about $S = 0.22$, 0.175 and 0.215, respectively. The corresponding values in the present study are $S = 0.213$, 0.174 and 0.193, with an uncertainty value within ± 0.01. Regarding

the S versus θ variation, there is one very notable distinction, though, that deserves to be emphasized: in the present study, exclusively for the critical angle θ_{c1}, in the vicinity of the separation of the wire-side shear layer, spectral analysis identifies a low value of Strouhal number S_L associated with a broad frequency peak, the centre of which has a low value (defined as f_L in figure 6) that is one order of magnitude smaller than the Kármán frequency; this low frequency or the associated low value of Strouhal number was not reported by Nebres (1992) and Nebres & Batill (1993). They determined, however, a critical angular position, denoted as θ_c, at which a steep drop in the value of Strouhal number S was encountered with an increase of the wire position by 1°; nevertheless this sudden drop occurred to a value of S that is of the same order of magnitude as the Kármán instability. Despite this significant difference, observation of an abrupt jump in the value of S suggests a possible correspondence between the critical angle θ_c defined by Nebres (1992) and Nebres & Batill (1993) and the critical angle θ_{c1} defined in the present investigation. The location of their measurements (1.64D from the cylinder axis) appears to be far away from the region, where the low frequency f_L prevails, and hence this might be the reason why f_L was not detected in their investigation. For further comments on the possible association of the two critical angles (θ_{c1} of the present investigation and θ_c of theirs), the reader is referred to the § 6.5 of Ekmekci (2006), where some commonly observed flow features are also addressed for the two independently defined critical cases; given those similarities, possible correspondence between the two independent results deserves further exploration.

In the present study, the technique of quantitative space–time imaging allows the definition of spectral analysis at a large number of points over the flow domain. The next section provides the characterization of this type over the entire near-wake region of the cylinder–wire system.

3.2.3. *Global patterns of spectra*

Insight into the unsteady flow phenomena affected by the surface wire is further enhanced through the whole-field representations of velocity spectra, determined at a total of 2400 locations in the near-wake flow region. During these global analyses, the prevailing frequency of the velocity fluctuation is found to take different values that depend on θ, as indicated in the S versus θ plot in figure 7. With this in mind, for a given value of θ, we decomposed the autospectral density $S_u(f)$ of the streamwise velocity u fluctuations in the global near-wake region into the following components of the spectrum: the low-frequency component f_L, and the three different values of Kármán frequency components f_{K1}, f_{K2} and f_{K3}; each one of these frequencies is specified, in figure 7, as the predominant frequency of velocity spectra for a given angular position θ of the wire. In figure 8, the contours of constant amplitude of these frequency-decomposed autospectra are presented for the critical positions $\theta_{c1} = 55°$ and $\theta_{c2} = 65°$, and for the $\theta = 120°$ position of the wire. The latter is shown, in the preceding sections, to be the angular position, where the wire does not exert any detectable influence on the near wake. In the layout of figure 8, each row provides representations of the frequency-decomposed autospecta at a different θ; and each column presents patterns corresponding to a given frequency of the autospectrum, i.e. the first column shows patterns of the low frequency f_L decomposition, and the second to fourth columns provide autospectra associated with the f_{K1}, f_{K2} and f_{K3} decompositions, respectively. For ease of comparison, the same contour levels are employed in all representations. At a given value of θ in figure 8, the contour pattern with the largest peak amplitude distinguishes

https://doi.org/10.1017/S0022112010003848 Published online by Cambridge University Press

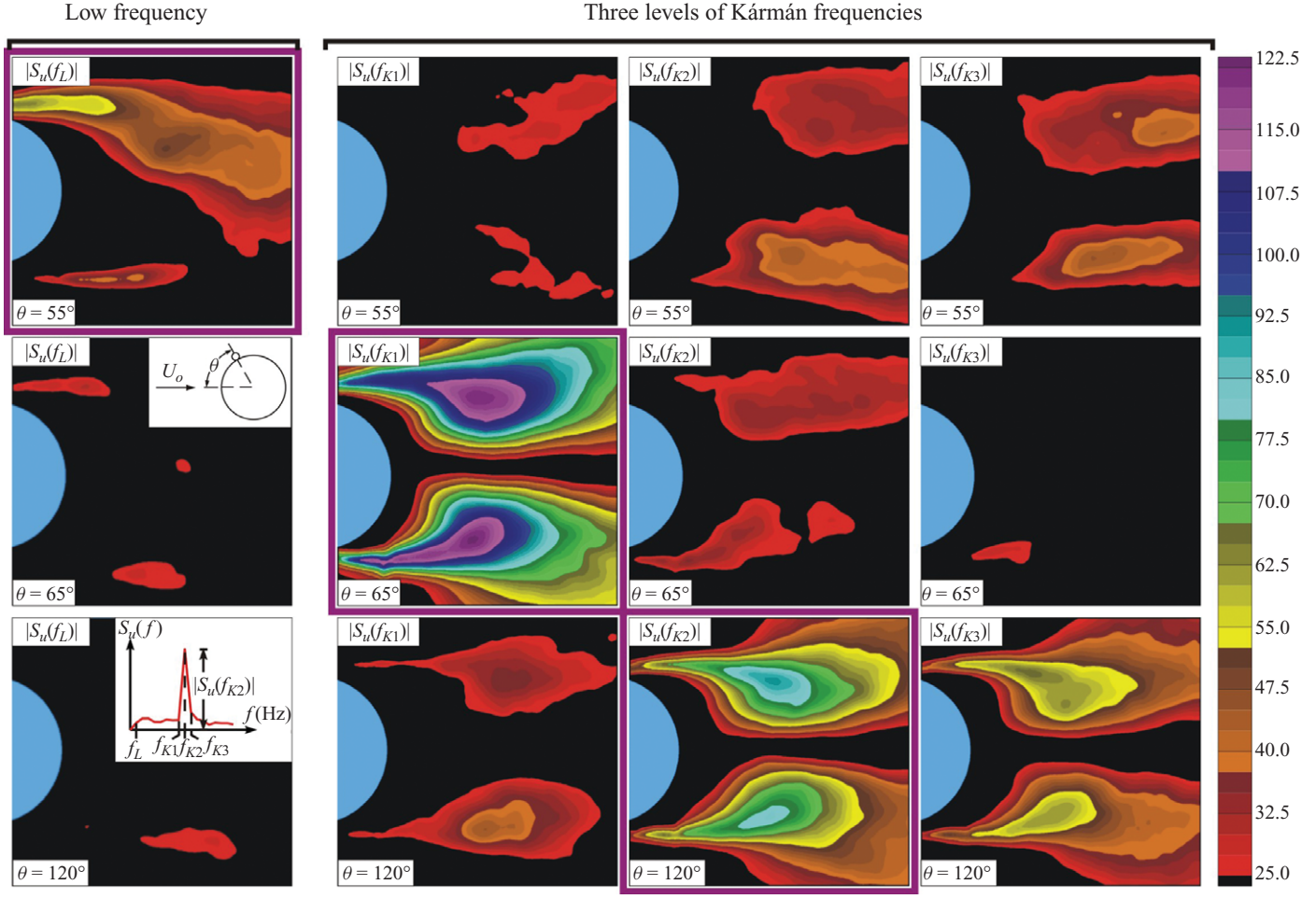

FIGURE 8. Contours of constant amplitude of autospectral density of fluctuating streamwise velocity u, decomposed into the low frequency f_L and the three levels of Kármán frequencies f_{K1}, f_{K2} and f_{K3}, which were defined in figure 7, are given at the wire angular positions $\theta = 55°$, $65°$ and $120°$, respectively. Minimum and incremental values are as follows: $[|S_u(f_i)|]_{min} = 25\,\mathrm{mm\,s^{-1}}$, $\Delta[|S_u(f_i)|] = 2.5\,\mathrm{mm\,s^{-1}}$, where $f_i = f_L$, f_{K1}, f_{K2}, f_{K3}.

the prevailing frequency component of the autospectrum $S_u(f)$. Accordingly, the prevailing frequency is the low frequency f_L (particularly on the wire side of the near wake) at $\theta_{c1} = 55°$, then f_{K1} dominates at $\theta_{c2} = 65°$, and it is f_{K2} at the reference position $\theta = 120°$. Framed patterns in figure 8 indicate those corresponding to these prevailing components.

At the first critical angle $\theta_{c1} = 55°$, spectral amplitudes of all the Kármán frequency (f_{K1}, f_{K2} and f_{K3}) decompositions are significantly attenuated over the entire near wake in comparison to the spectral amplitude at the predominant Kármán frequency (f_{K2}) of the reference case at $\theta = 120°$. This observation reinforces the attenuation of the Kármán instability at $\theta_{c1} = 55°$, as shown in figure 6. A further aspect, which occurs at $\theta_{c1} = 55°$ in figure 8, involves the contour plot of $|S_u(f_L)|$. This plot clearly shows that the unsteadiness in the upper shear layer on the wire side of the near wake, especially at and downstream of separation, is dominated by the fluctuation at the low frequency f_L. Due to the mutual interaction of the shear layers, a detectable influence of this component f_L is also present in the lower shear layer on the smooth side of the near wake. These findings related to the low-frequency fluctuations at $\theta_{c1} = 55°$ are also in good agreement with those of figure 6.

In figure 8, at the second critical angle $\theta_{c2} = 65°$ of the wire, we observe that the peak spectral amplitude of the predominant Kármán frequency f_{K1} is relatively high in comparison to the peak amplitude at the predominant Kármán frequency f_{K2} of the reference case at $\theta = 120°$. This implies that the wire at $\theta_{c2} = 65°$ further intensifies the instability of Kármán vortex shedding, in accord with what was deduced previously from figure 6 based on the spectra at a number of points in the near wake.

Figure 9 provides, over the entire range of θ from 40° to 120°, patterns of constant amplitude of autospectral density associated with the streamwise velocity u fluctuation at the prevailing frequency of the Kármán instability. In addition, figure 10 gives corresponding contour plots associated with the transverse velocity v fluctuation. Peak amplitudes of these $S_u(f)$ and $S_v(f)$ plots can be viewed as indirect indicators of relative coherence and strength of the periodic Kármán vortex shedding at each value of θ. From simultaneous consideration of the layouts of figures 9 and 10, it is clear that, for increasing angular position of the wire from $\theta = 40°$ up to $\theta_{c1} = 55°$, the peak amplitudes, and hence the coherence and strength of the Kármán instability, gradually decrease, eventually showing the previously noted attenuation at $\theta_{c1} = 55°$. As θ is increased beyond the first critical angle $\theta_{c1} = 55°$ up to the second critical angle $\theta_{c2} = 65°$, the peak amplitudes gradually increase and reach the highest relative value at $\theta_{c2} = 65°$, thereby indicating the highly coherent primary instability, which was also evident in the frequency-decomposed autospectra plots of figure 8. For $\theta > 65°$, the spectral peaks have smaller amplitudes than the peaks at $\theta_{c2} = 65°$. At $\theta = 80°$, however, peaks with relatively large amplitude arise again. This rise further suggests a third critical angle at $\theta = 80°$.

3.2.4. *Instantaneous patterns of the near wake*

We now address the temporal evolution of the flow structure in the near wake, with the aim of gaining further insight into the unsteady flow characteristics. Sequential patterns of instantaneous vorticity $|\omega|D/U_o$ are shown in figure 11, where the time interval between the successive images is approximately one-half of the nominal period T_K of the Kármán vortex formation. These patterns are provided for the angular positions (i) $\theta_{c1} = 55°$, (ii) $\theta_{c2} = 65°$ and (iii) $\theta = 120°$ of the wire. As indicated in the foregoing, these angular positions are associated, respectively, with: (i) extension of the near wake, attenuation of the Kármán vortex shedding, and onset of fluctuating

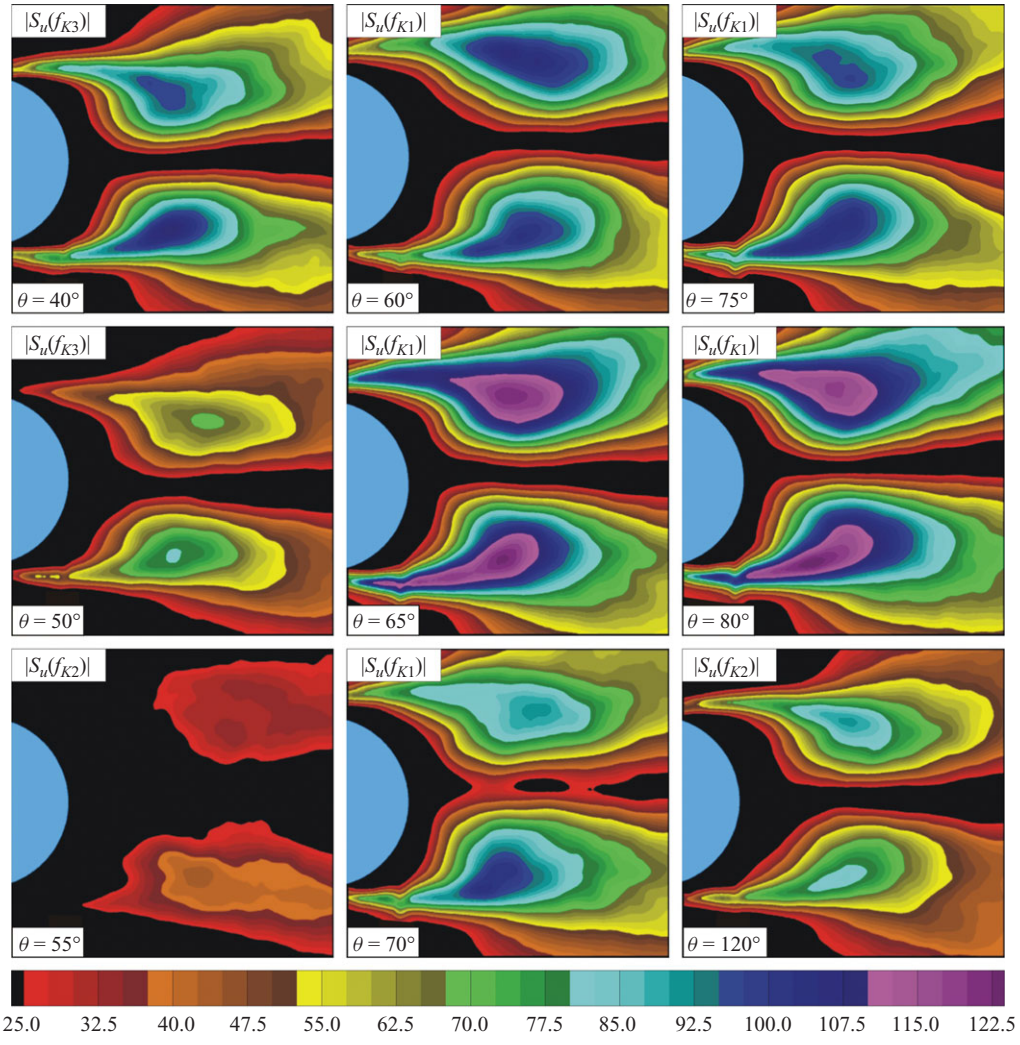

FIGURE 9. Contour patterns of peak amplitude of autospectral density corresponding to the streamwise velocity component u at the respective Kármán frequency of different angular positions of the wire ranging from $\theta = 40°$ to 120°. Minimum and incremental values are as follows: $[|S_u(f_i)|]_{min} = 25\,\mathrm{mm\,s^{-1}}$, $\Delta[|S_u(f_i)|] = 2.5\,\mathrm{mm\,s^{-1}}$, where $f_i = f_{K1}, f_{K2}, f_{K3}$.

activity at a low frequency in the wire-side shear layer; (ii) contraction of the near wake, and enhancement of the coherence and strength of the Kármán vortex shedding; (iii) a reference case at which the near-wake structure is not markedly affected by the surface wire. In all patterns of figure 11, absolute values of the normalized vorticity $|\omega|D/U_o$ are plotted in order to allow direct comparison of the structure of the opposite shear layers.

The top row of figure 11 shows images of instantaneous vorticity $|\omega|D/U_o$ at $\theta_{c1} = 55°$. From inspection of these patterns, formation of large-scale clusters of vorticity is evident, but there is no indication of rhythmic development of these clusters from one snapshot to the next. That is, ordered and consistent shedding of Kármán vortices cannot be detected for this particular critical angle θ_{c1}. This observation is in accord with the foregoing observation, where attenuation of the

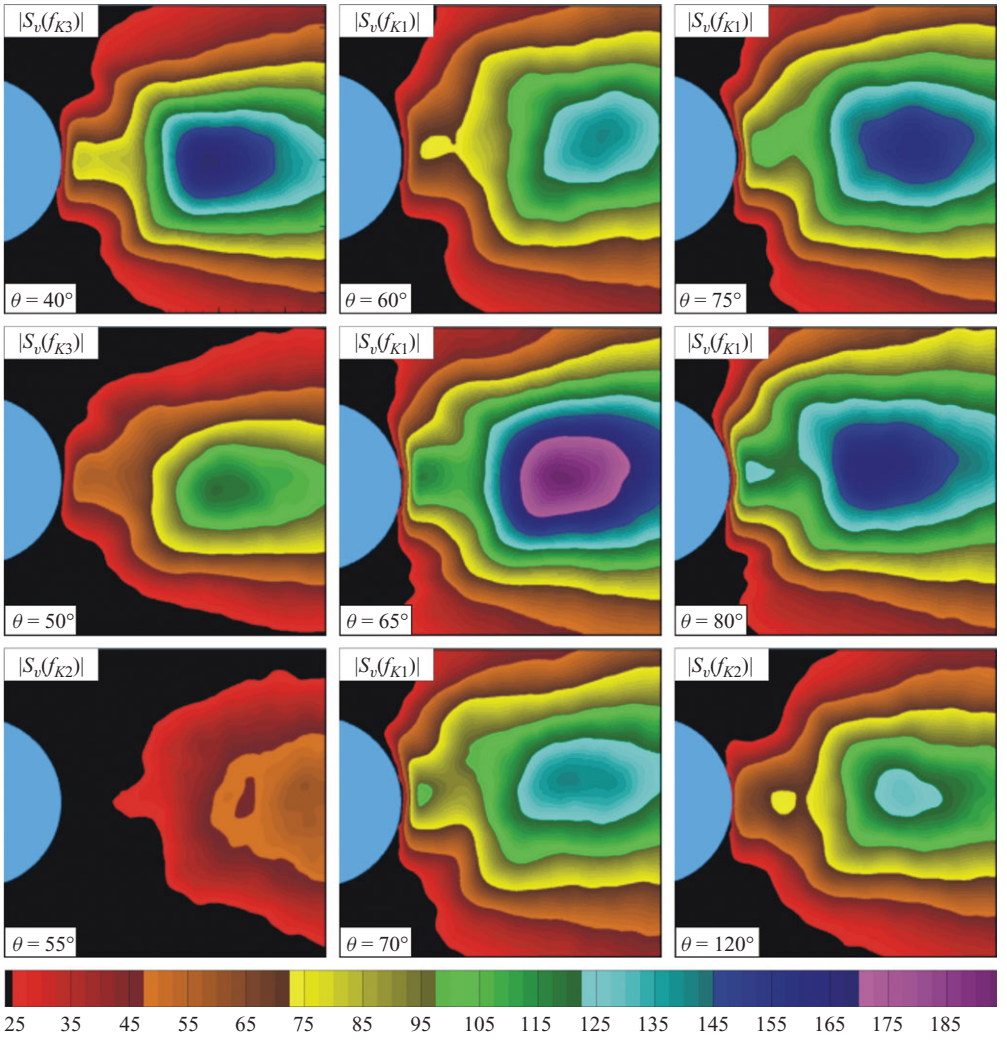

FIGURE 10. Contour patterns of peak amplitude of autospectral density corresponding to the transverse velocity component v at the respective Kármán frequency for different angular positions of the wire ranging from $\theta = 40°$ to 120°. Minimum and incremental values are as follows: $[|S_v(f_i)|]_{min} = 25\,\mathrm{mm\,s^{-1}}$, $\Delta[|S_v(f_i)|] = 2.5\,\mathrm{mm\,s^{-1}}$, where $f_i = f_{K1}, f_{K2}, f_{K3}$.

Kármán instability at θ_{c1} is deduced via comprehensive analysis of velocity spectra. A further point involves small-scale concentrations of vorticity, evident in the separating shear layers. These concentrations start to form considerably earlier in the upper (wire-side) shear layer compared to those in the lower (smooth-side) shear layer, suggesting that the wire at $\theta_{c1} = 55°$ promotes earlier onset of instability in the separating shear layer. A corresponding animation is also available online (see movie 1 available at journals.cambridge.org/flm). The middle row of patterns in figure 11 represents the angular position $\theta_{c2} = 65°$ of the wire. Large-scale clusters of vorticity associated with the highly-coherent process of Kármán vortex shedding are evident from the smooth side of the cylinder in the first and third images and from the wire side of the cylinder in the second image. Again, small-scale concentrations of

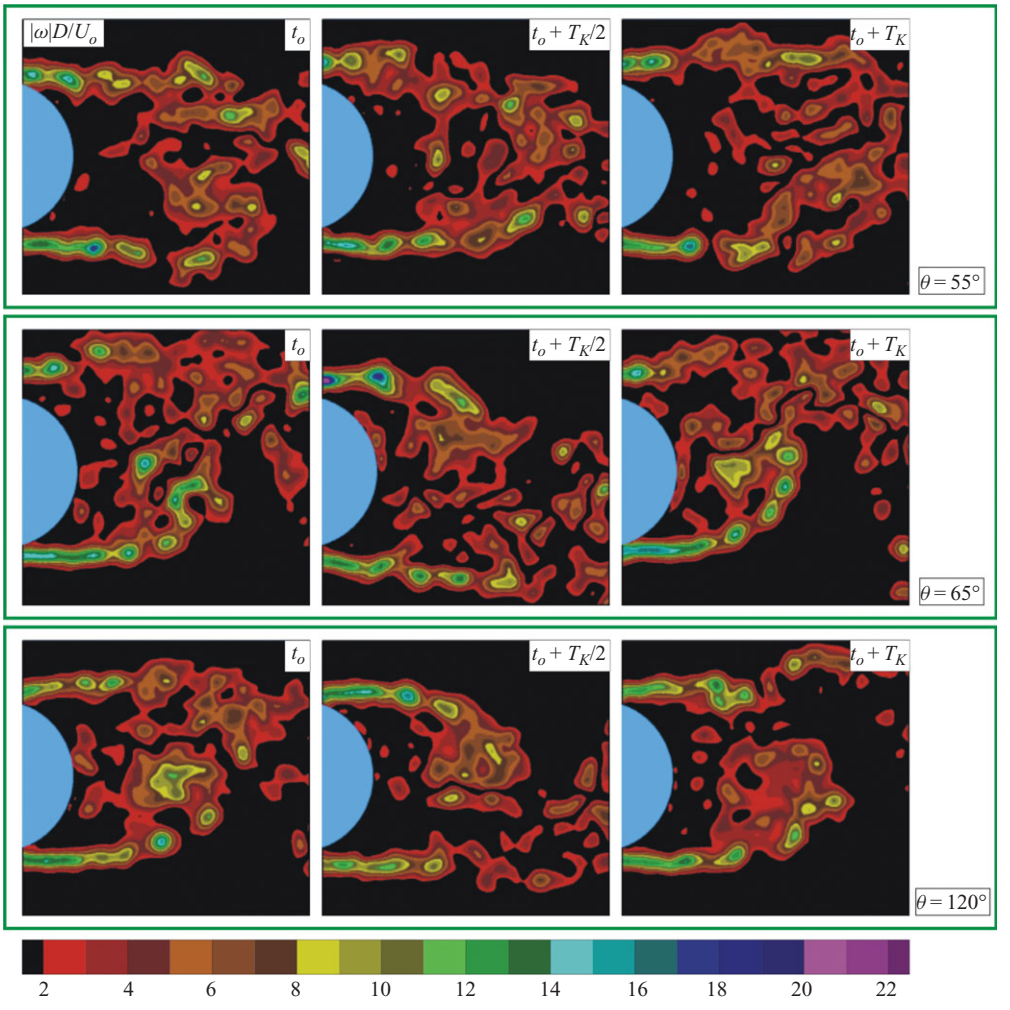

FIGURE 11. Instantaneous vorticity contours at the wire angular positions $\theta = 55°$, 65° and 120°. Absolute values of normalized vorticity are plotted for purposes of comparison of the shear layers. Minimum and incremental values are as follows: $[|\omega|D/U_o]_{min} = 2$ and $\Delta[|\omega|D/U_o] = 1$. Time interval between the images corresponding to $\theta = 65°$ and 120° is one half the respective period T_K of the Kármán shedding. At $\theta = 55°$, it is approximately one-half the nominal Kármán period of other values of θ since ordered Kármán shedding does not occur at this angle of the wire. Corresponding animations at the critical wire positions $\theta = 55°$ and 65° are also available online (see movies 1 and 2).

vorticity form much earlier in the wire-side shear layer. A corresponding animation for the case of $\theta_{c2} = 65°$ can also be found online (see movie 2). The third row of figure 11 corresponds to the reference case when the location of the wire is at $\theta = 120°$. Coherent formation of large-scale Kármán vortices is clearly evident for this case. In addition, vorticity patterns remain elongated downstream of separation and it is generally not until further downstream locations that the small-scale concentrations appear in both wire-side and smooth-side shear layers, indicating no influence of the wire at this particular angle on the onset of shear-layer instability.

An important interpretation of the aforementioned observations at the critical angles (θ_{c1} and θ_{c2}) is that the unsteadiness associated with the earlier onset of small-scale vortical structures on the wire side is the source of distortion of the time-averaged near wake, observed in figures 2–5. Further insight into the effect of the wire on the onset of shear-layer instability, and its variation with θ, will be addressed in detail in a subsequent section.

4. Shear-layer structure

In § 3, the variation of the flow structure with angular position θ of the wire was described, with an emphasis on the downstream region of the two separating shear layers. This section will focus only on the structure of the upstream region of the wire-side shear layer, and the manner in which it changes with θ; this flow structure was determined from a separate set of PIV experiments.

4.1. *Global spectra*

The global spectral analyses herein provide physical insight into the flow domain that is upstream of the unsteady shear layer separating from the wire side of the cylinder, as well as means of verification of the spectral characteristics, given in the preceding section. Figure 12 shows contours of constant amplitude of frequency-decomposed autospectra for wire locations at the critical angles $\theta_{c1} = 55^\circ$ and $\theta_{c2} = 65^\circ$, and at the reference angle $\theta = 120^\circ$. Therein, the spectral decompositions are performed into the four frequency components (f_L, f_{K1}, f_{K2} and f_{K3}) in the same manner as in those given in figure 8. If we recall the S versus θ variation of figure 7, each of these frequency components becomes predominant at a given value of θ. For each value of θ in figure 12, the framed pattern identifies the decomposition at the predominant frequency.

The first row of figure 12 corresponds to $\theta_{c1} = 55^\circ$. At this critical angle, the spectral components at the Kármán vortex shedding frequency (f_{K1}, f_{K2} and f_{K3}) barely exceed the background level, especially when compared with the reference case at $\theta = 120^\circ$, given in the third row. This is a clear indication of attenuation of the Kármán instability in the vicinity of the cylindrical body. Furthermore, low-frequency fluctuations dominate at this critical angle, apparent from the large-amplitude peak at the f_L decomposition. All these observations at $\theta_{c1} = 55^\circ$ are in accord with the conclusions reached through spectral analyses of the overall near wake, presented in § 3.

The set of decomposed autospectra in the second row of figure 12 corresponds to $\theta_{c2} = 65^\circ$. The predominant Kármán frequency f_{K1}, in this case, shows a relatively large peak amplitude in comparison to the peak amplitude at the predominant frequency f_{K2} of the case of $\theta = 120^\circ$. Hence, once again, it is clear that the wire at $\theta_{c2} = 65^\circ$ intensifies the Kármán instability.

The physical origin of the pronounced low-frequency fluctuations, which are encountered only when the wire is at the critical position $\theta_{c1} = 55^\circ$, has not yet been clarified. This phenomenon is addressed in the next section, using phase-averaged patterns of the shear layer.

4.2. *Phase-averaged oscillations of the separating shear layer*

An important aspect of the separated shear layer is its oscillation in the transverse direction, designated as shear-layer flapping. In this section, the oscillating shear layer is characterized at the two limiting positions of its flapping motion, i.e. the uppermost and the lowermost deflections. Figure 13 shows phase-averaged contour plots of

https://doi.org/10.1017/S0022112010003848 Published online by Cambridge University Press

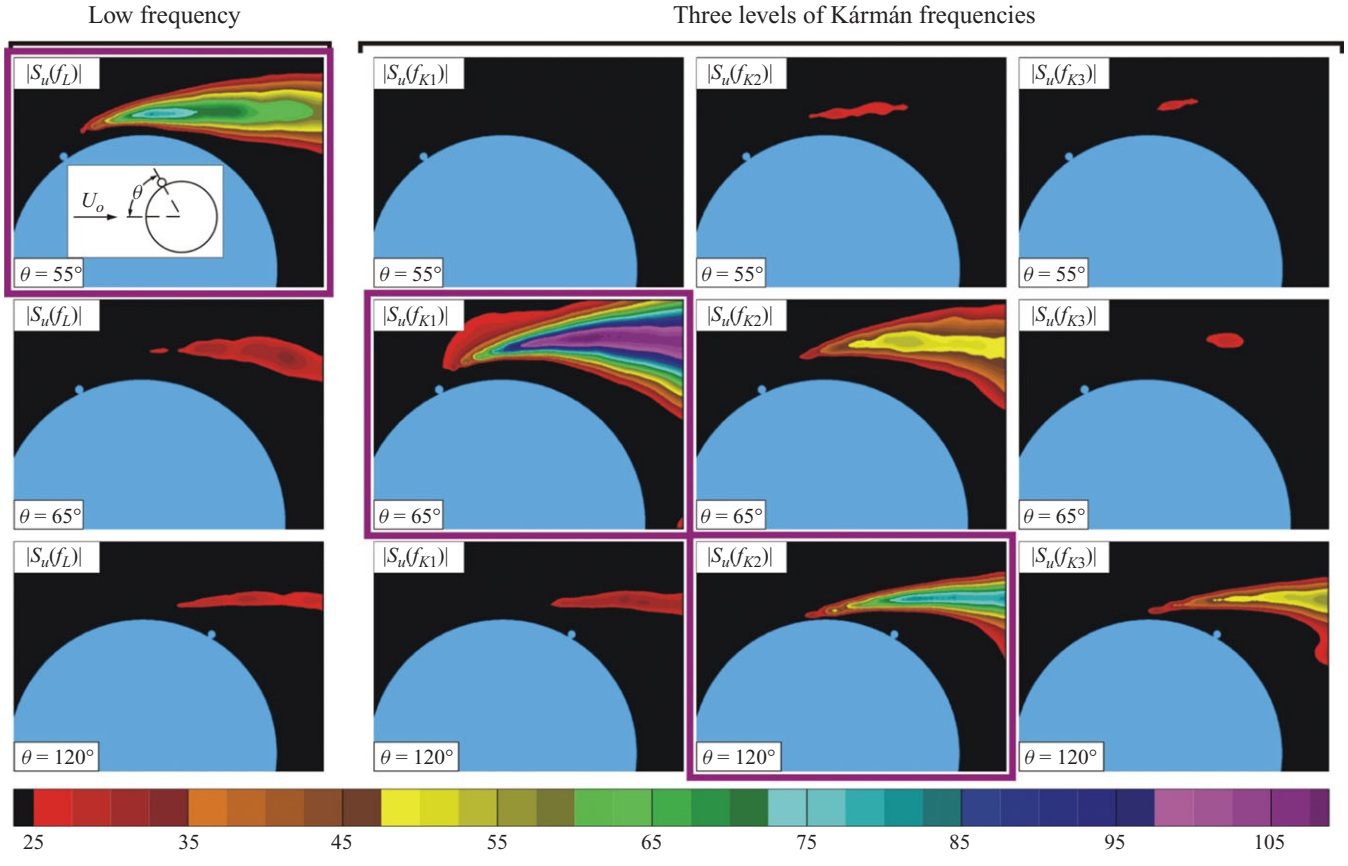

FIGURE 12. Contours of constant amplitude of autospectral density of fluctuating streamwise velocity u, decomposed into the low frequency f_L and the three levels of Kármán frequencies f_{K1}, f_{K2} and f_{K3}, which were defined in figure 7, are given at the critical angular positions $\theta = 55°$ and $65°$ and the reference position $\theta = 120°$ of the wire. Minimum and incremental values are as follows: $[|S_u(f_i)|]_{min} = 25\,\mathrm{mm\,s^{-1}}$, $\Delta[|S_u(f_i)|] = 2.5\,\mathrm{mm\,s^{-1}}$, where $f_i = f_L, f_{K1}, f_{K2}, f_{K3}$.

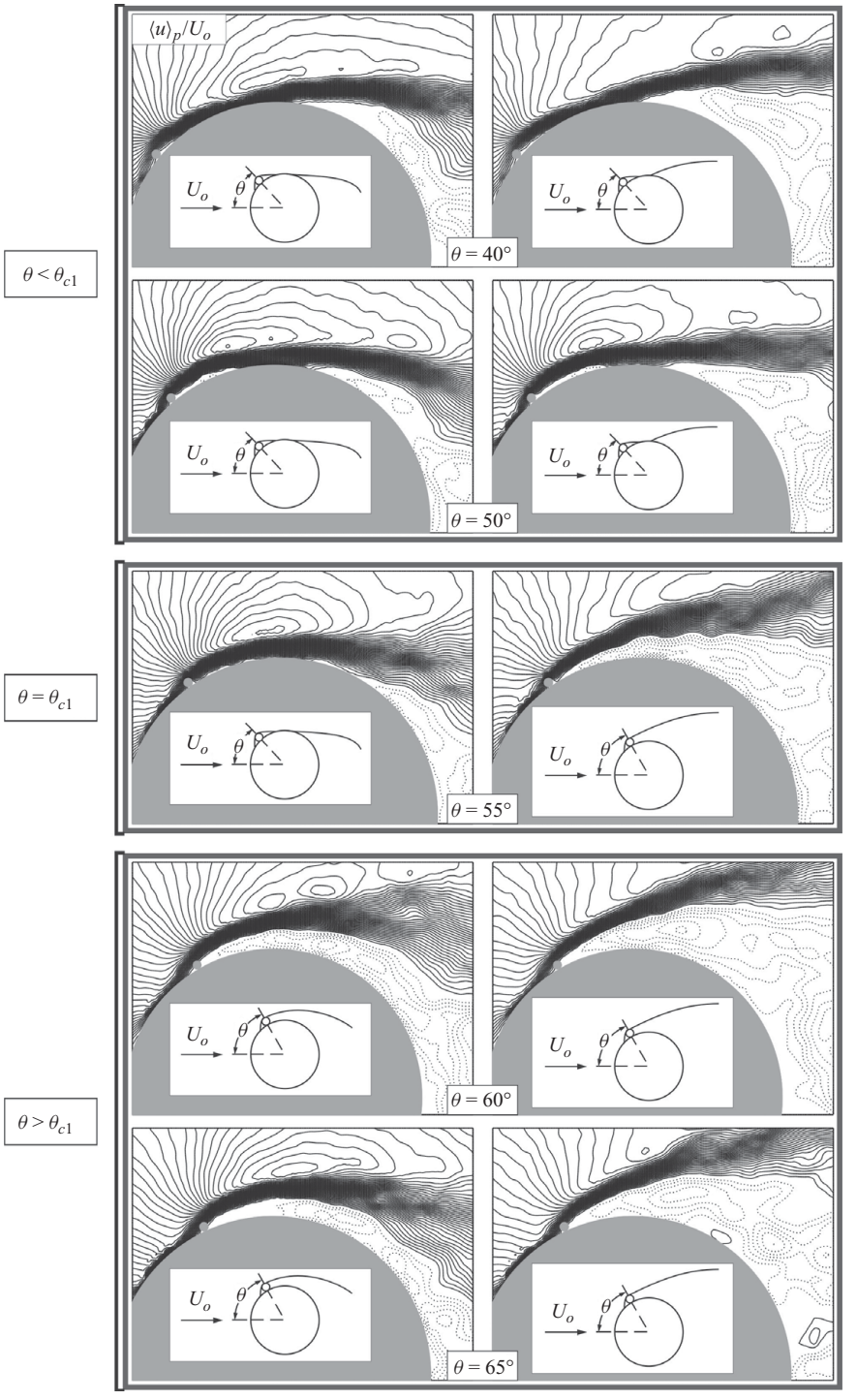

FIGURE 13. Patterns of phase-averaged streamwise velocity $\langle u\rangle_p/U_o$ for angular positions before, at and after the critical angle θ_{c1}. Phase-averaging is applied to the instantaneous patterns that are selected from the successive lowermost and uppermost shear-layer positions during its transverse oscillations. Minimum and incremental values are as follows: $|[\langle u\rangle_p/U_o]|_{min} = 0.04$ and $\Delta|[\langle u\rangle_p/U_o]| = 0.04$.

streamwise velocity $\langle u \rangle_p / U_o$ at values of θ that are smaller than θ_{c1} (at $\theta = 40^\circ$ and 50°), equal to $\theta_{c1} = 55^\circ$, and larger than θ_{c1} (at $\theta = 60^\circ$ and 65°). In the layout of this figure, patterns corresponding to each value of θ are provided in a row, where the left image is the average of the lowermost deflections, while the right image is the average of the uppermost deflections. For visual clarity, the mode of deflection is schematically illustrated in the inset of each pattern. We should emphasize here that, in the contour patterns of $\langle u \rangle_p / U_o$, the positive values are indicated by solid lines, and the negative values are represented by broken lines. Therefore, in these plots, the separating shear layer can be distinguished by the dense region of solid lines.

Patterns of $\langle u \rangle_p / U_o$ in figure 13 reveal that, at values of $\theta < \theta_{c1}$, i.e. $\theta = 40^\circ$ and 50°, for both the lowermost and uppermost deflections, the shear layer separates at the wire, then reattaches to the cylinder surface, and the final separation takes place from the cylinder at a further downstream location. This mode of separation is also evident in movie 3 with the online version over the entire temporal evolution of the shear-layer flapping. In contrast, at values of $\theta > \theta_{c1}$, i.e. $\theta = 60^\circ$ and 65°, at both of its extreme deflections, the shear layer in figure 13 shows a complete separation at the wire, that is, no reattachment is observed. Movie 5 with the online version clearly shows this mode of separation. On the other hand, at the critical angle $\theta_{c1} = 55^\circ$, the shear layer in figure 13 shows two distinct modes of separation. At one extreme, the separating shear layer reattaches after the wire and then separates from the cylinder surface. At the other extreme, it separates at the wire with no reattachment afterwards. Oscillation of the shear layer between these two modes of separation can also be seen in movie 4 with the online version.

The spectra of streamwise velocity fluctuations, addressed in several preceding sections, suggest that both at $\theta < \theta_{c1}$ and $\theta > \theta_{c1}$, the shear-layer flapping occurs at the characteristic frequency of the Kármán vortex shedding. That is, for example, the shear layer flaps at f_{K3} when the wire is located at $\theta = 40^\circ$ or 50° and at f_{K1} when it is at $\theta = 60^\circ$ or 65°. On the other hand, when the surface wire is at the critical angle ($\theta = \theta_{c1}$), the shear layer oscillates between the two extreme states, which have different modes of separation, at low values of frequency, centred at f_L.

4.3. *Bistable instability*

Based on the separation mode of the shear layer, deduced from the phase-averaged patterns given in figure 13 as well as the representative movies (3–5) available with the online version, it is possible to define principal flow states relative to the critical angle θ_{c1}. As illustrated in figure 14, these states can be classified into three categories.

(i) Stable state I: at $\theta < \theta_{c1}$, separation of the shear layer at the wire is followed by a steady reattachment and an eventual separation from the cylinder surface.

(ii) Stable state II: at $\theta > \theta_{c1}$, the shear layer, which separates at the wire, remains separated.

(iii) Bistable state: at $\theta = \theta_{c1}$, a bistable situation occurs, such that the separating shear layer oscillates between the stable state I and stable state II at broad low frequencies, centred at f_L.

Accordingly, the low-frequency unsteadiness in the wire-side shear layer, encountered only when the surface wire is at the critical position θ_{c1}, is associated with bistable behaviour. A survey of the literature shows that similar bistable flow oscillations have been documented for a variety of fluid-dynamic configurations, such as flow through diffusers (Fox & Kline 1960; Smith & Kline 1974; Smith 1975), flow past prisms (Rockwell 1977; Wedding *et al.* 1978), flow past backward-facing steps (Eaton & Johnston 1980, 1981), flow past leaf gates (Narayanan & Reynolds

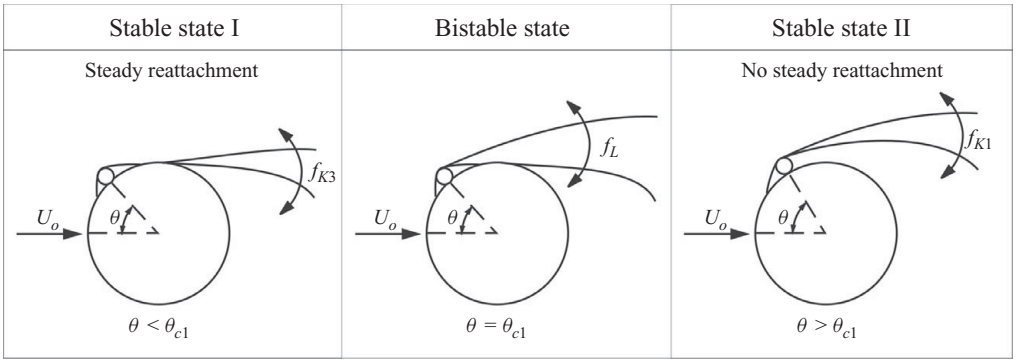

FIGURE 14. Bistable instability for flow around cylinder–wire arrangement. Schematic illustrates flow regimes before, at and after the critical angular position θ_{c1} of the wire. The two extreme positions of shear-layer flapping are represented for each regime via lines. f_{K3} and f_{K1} are the characteristic Kármán frequencies for $\theta < \theta_{c1}$ and $\theta > \theta_{c1}$, respectively, and f_L is the low frequency. (The size of the wire relative to the size of the cylinder is exaggerated in the schematic for demonstration purposes.)

1968), wall jets (Bourque & Newmann 1960; Newman 1961) and flow past/through a variety of other configurations of hydraulic structures (Nikitina & Kulik 1980). It may be worthwhile to point out here the fundamental features that are common to all oscillatory flows in the bistable category, including the present bistable regime.

First, a typical common feature is that the entire shear layer oscillates, relative to the adjacent structure, around a (time-averaged) equilibrium position, rather than short-wavelength undulations within that shear layer associated with a classical hydrodynamic instability.

Second, there typically exist variations in the volume V enclosed within a separation bubble due to an imbalance of mass flow. For the present case, the flow separation at the wire leads to formation of a mean dividing streamline, which borders the separation bubble and bifurcates at the reattachment point into two branches: one branch forms the new boundary layer; the other branch flows backwards and contributes to the recirculation bubble behind the wire. The latter, with a volumetric flow rate of Q_R, tends to enlarge the recirculation bubble; while the former, the fluid entrainment into the separated shear layer with a volumetric flow rate Q_E, tends to shrink this bubble. The bistable oscillation of the shear layer is a consequence of a bistable variation in the volume V of the recirculation bubble due to an imbalance between these two flow rates. This can be expressed as

$$\mathrm{d}V/\mathrm{d}t = Q_R - Q_E. \tag{4.1}$$

Third, bistable flow oscillations are intermittent, rather than periodic, and therefore are generally less dangerous to a structure than most other instability-induced oscillations (Naudascher & Rockwell 2005). A distinguishing characteristic is that these oscillations occur over a broad range of low frequencies with a defined centre frequency that is one to two orders of magnitude smaller than those of the characteristic instabilities (Naudascher & Rockwell 2005). In the present cylinder–wire configuration, the frequency of the bistable instability is indeed broad in nature and its nominal value is one order of magnitude smaller than the characteristic Kármán frequency f_K. Our longer-time cinematographic records of the shear layer, which

are elaborated in Ekmekci (2006), also verified clearly the intermittency of bistable oscillations.

In the following, patterns of the instantaneous structure of the separating shear layer are presented for varying angular position θ of the wire, with the aim of providing further insight into the unsteady aspects.

4.4. *Instantaneous structure of the shear layer*

4.4.1. *Instantaneous streamwise velocity*

To characterize the spatial extent of the shear-layer flapping as a function of the angular position θ of the wire, figure 15 presents superposed contour patterns of instantaneous streamwise velocity u/U_o arising at extreme upper and lower deflections of the shear layer. In this layout, the contours at the upper shear-layer position are indicated in red and the contours at the lower position are in black. In addition, positive values of u/U_o are represented by solid lines and the negative values by broken lines. Hence, in the images, the dense region of solid lines indicates the shear layer. From the spectral analyses presented in the previous sections, we already know that, at all values of θ except $\theta_{c1} = 55°$, the shear layer oscillates between the two extreme positions at the characteristic Kármán frequency f_K. Only at $\theta_{c1} = 55°$, there is intermittent flapping of the shear layer at low frequencies, centred at f_L, which is an order of magnitude smaller than the characteristic Kármán frequency f_K.

In the layout of figure 15, we see representations of the shear-layer separation modes, defined in figure 14. That is, superposed patterns of u/U_o at all $\theta < \theta_{c1}$ ($\theta = 40°$ and 50°) exhibit the stable state I, featuring steady reattachment of the shear layer after the initial separation at the wire. At $\theta > \theta_{c1}$ (from $\theta = 60°$ to 80°), the stable state II occurs, with no reattachment of the shear layer. The critical angle $\theta_{c1} = 55°$ clearly shows the bistable state between the stable states I and II. At $\theta = 120°$, the wire is within the base region of the cylinder and shows no significant influence on the separation process of the shear layer.

From the layout of figure 15, it is evident that the spatial extent of the shear-layer flapping changes with θ. At $\theta = 40°$ and 120°, it has moderate amplitudes. As the angular position of the wire is increased, starting from $\theta = 40°$ towards the second critical angle $\theta_{c2} = 65°$, the extreme locations of the shear layer become further apart, indicating a gradual increase of the flapping amplitude. The wire at the first critical angle $\theta_{c1} = 55°$ also results in large-amplitude oscillations, due to the bistable condition. As θ is increased beyond $\theta_{c2} = 65°$, the deflections become smaller, and finally, at $\theta = 120°$, they are substantially reduced. Interestingly, at $\theta = 80°$, the deflections of the shear layer are smallest. These observations reveal that as the wire location approaches the second critical angle $\theta_{c2} = 65°$, which was shown in the foregoing to enhance the amplitude of the Kármán instability, the shear layer flaps over an increased transverse extent.

At and around the second critical angle $\theta_{c2} = 65°$, a further interesting observation concerns the instantaneous thickness of the shear layer. It becomes relatively large. The corresponding patterns of vorticity, provided in the following section, provide clarification of this observation.

4.4.2. *Instantaneous vorticity*

It is of interest to determine if the angular position of the wire affects the onset of small-scale vortical structures in the separated shear layer, which arise from the Kelvin–Helmholtz instability. Figure 16 shows instantaneous images of vorticity $\omega D/U_o$ corresponding to the lowermost deflection of the shear layer, over the range

https://doi.org/10.1017/S0022112010003848 Published online by Cambridge University Press

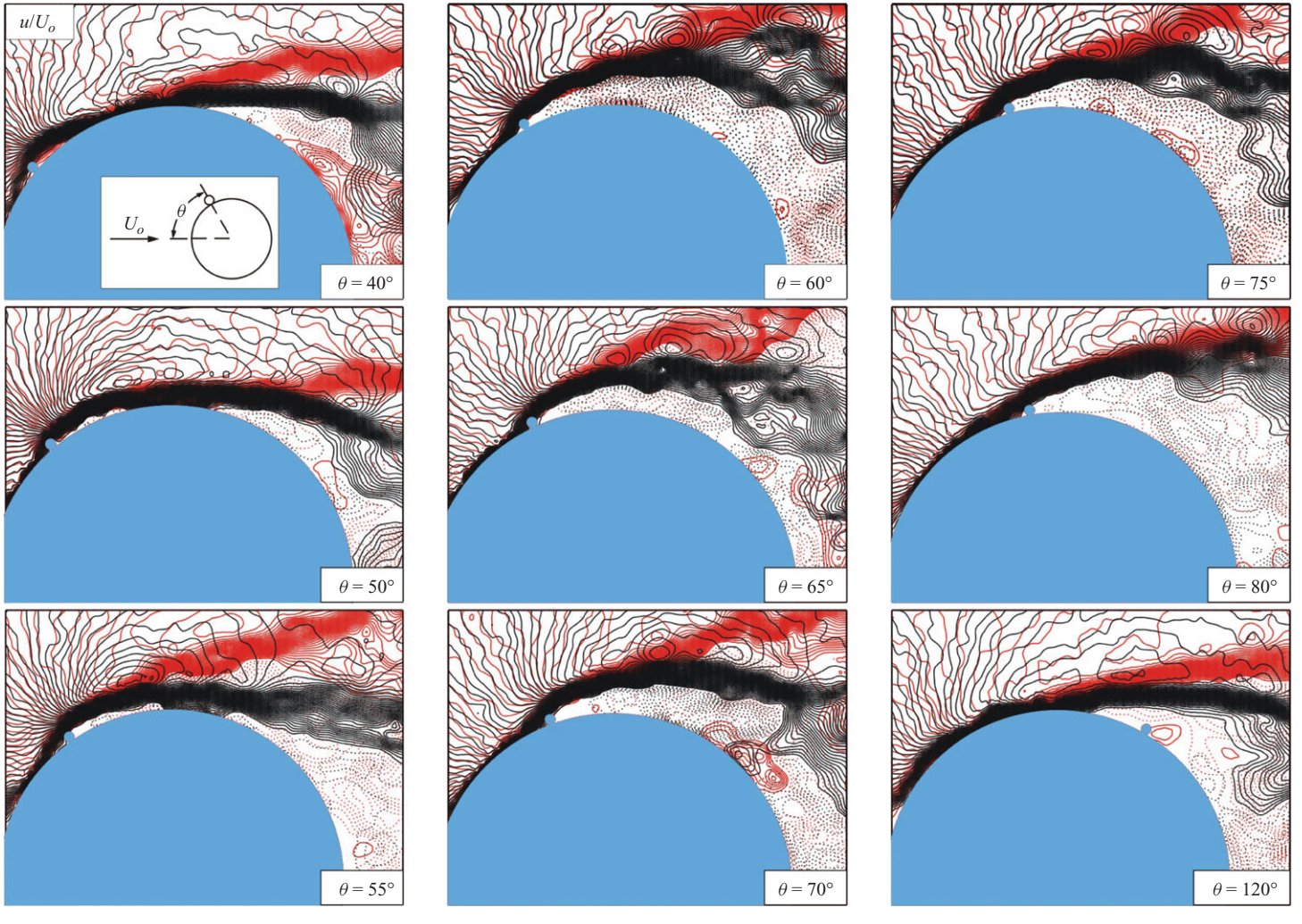

FIGURE 15. Patterns of instantaneous streamwise velocity u/U_o for angular positions of the wire ranging from $\theta = 40°$ to 120°. Images of successive lowermost (black) and uppermost (red) shear-layer positions in flapping motion are superposed to illustrate the transverse extent of flapping. Minimum and incremental values are as follows: $|[u/U_o]|_{min} = 0.04$ and $\Delta|[u/U_o]| = 0.04$.

https://doi.org/10.1017/S0022112010003848 Published online by Cambridge University Press

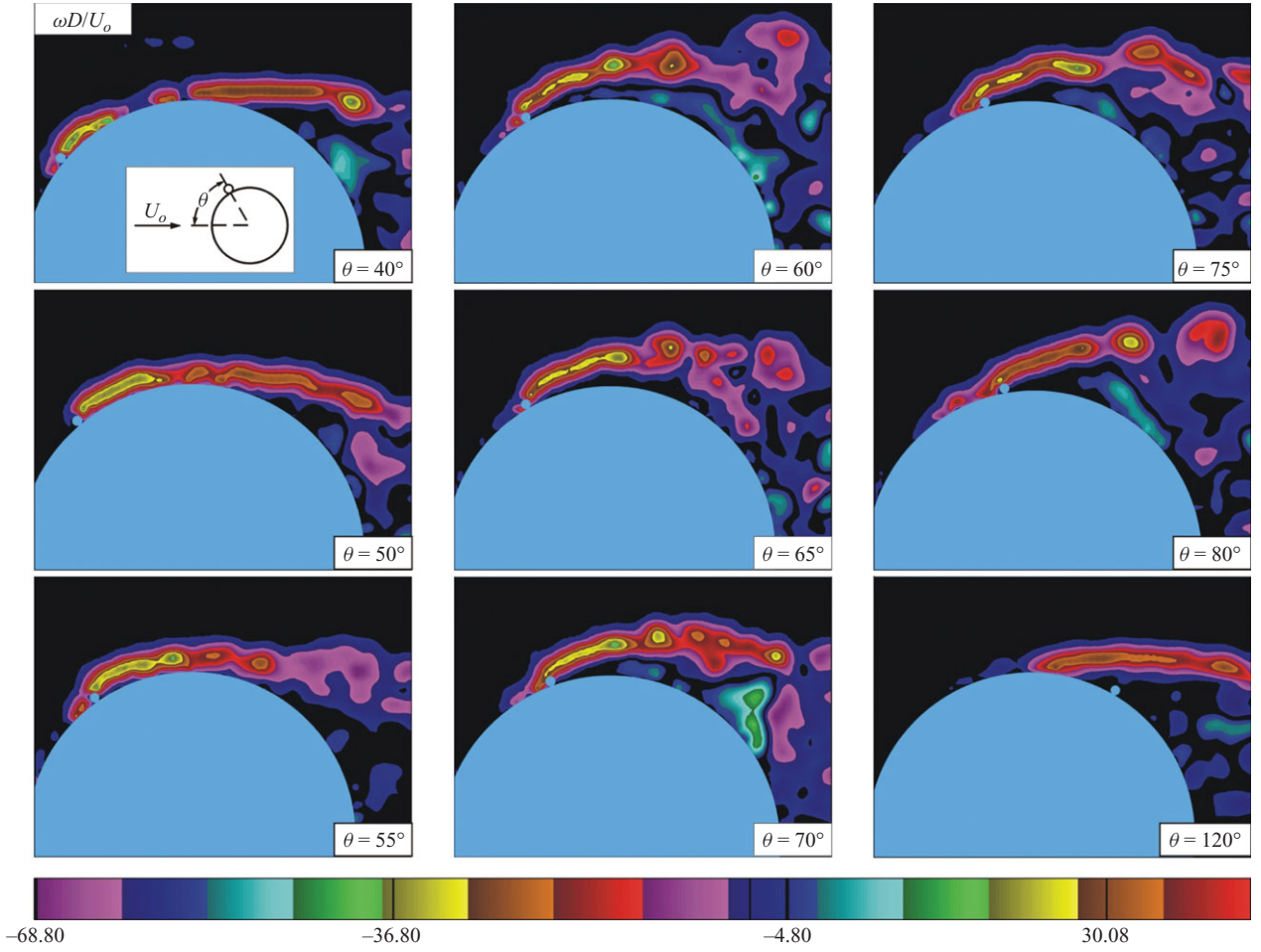

FIGURE 16. Patterns of instantaneous vorticity contours $\omega D/U_o$ for angular positions of the wire ranging from $\theta = 40°$ to 120°. Images are representative of the lowermost position of the shear layer. Minimum and incremental values are as follows: $|[\omega D/U_o]|_{min} = 1.6$ and $\Delta|[\omega D/U_o]| = 0.32$.

of θ from 40° to 120°. It is clear that the location of onset of small-scale vortical structures in the separated shear layer strongly depends on θ. At $\theta = 40°$ and 120°, the separated shear layer appears to remain elongated over a longer streamwise distance and the onset of the small-scale vortical structure occurs further downstream, in comparison to other angular positions of the wire. As addressed in § 3, wire locations $\theta = 40°$ and 120° induce negligible change of the near wake. Furthermore, figure 16 shows that, over the range of θ, at the first critical angle $\theta_{c1} = 55°$, and at and in the vicinity of the second critical angle $\theta_{c2} = 65°$, the onset of small-scale vortical structures is notably advanced upstream. In addition, especially for angles at and around the second critical angle $\theta_{c2} = 65°$, the instantaneous thickness of the shear layer is increased as a result of earlier coalescence of the small-scale vortices within the shear layer. As the angular position of the wire is increased to values well beyond $\theta_{c2} = 65°$, the streamwise location of the onset of small-scale vortices gradually moves downstream, finally reaching the furthest downstream location at $\theta = 120°$.

It should be noted here that the intermittent streamwise movement of the transition point in the shear layer is a well-known phenomenon for flow past a smooth cylinder, as addressed in the investigations of Cardell (1993) and Prasad & Williamson (1997), amongst others. Similar intermittent fluctuations in the onset location of small-scale vortical structures are observed in the present investigation for the cylinder–wire configuration. Details are described by Ekmekci (2006), where the timewise evolution of $\omega D/U_o$ is provided at each value of θ.

4.4.3. *Instantaneous Reynolds stress*

Figure 17 illustrates the contour patterns of instantaneous Reynolds stress correlation $u'v'/U_o^2$ at the lowermost deflection of the shear layer. These instantaneous images directly correspond to the patterns of $\omega D/U_o$ given in figure 16. It is evident that, when the angular position θ of the wire is at or in the vicinity of the second critical angle $\theta_{c2} = 65°$, small-scale cell-like concentrations of Reynolds stress prevail at upstream locations in the separating shear layer. As the angular position of the wire recedes away from $\theta_{c2} = 65°$, and approaches the angular position of either $\theta = 40°$ or 120°, the small-scale $u'v'/U_o^2$ concentrations commence at locations further downstream in the shear layer. In a general sense, these small-scale cell-like concentrations of Reynolds stress $u'v'/U_o^2$ are most likely associated with the small-scale vortical structures addressed in figure 16, as they occur at proximate locations at the respective values of θ.

Taken together, figures 16 and 17 bring forth the following physics of the separated shear layer at the second critical angle $\theta_{c2} = 65°$. Early onset of small-scale vortical structures in the shear layer that separates from the wire is associated with an early increase of Reynolds stress, which gives rise to an increase in the entrainment demand of the shear layer. This demand, in turn, is satisfied by the flow from the mean recirculation region of the near wake, resulting in the so-called near-wake contraction, as observed in the time-averaged patterns of the near-wake structure at $\theta_{c2} = 65°$ in figures 2 and 3.

In the following, the foregoing findings, represented by instantaneous patterns, are complemented by time-averaged patterns.

4.5. *Time-averaged structure of the shear layer*

4.5.1. *Time-averaged streamline topology*

Patterns of time-averaged streamline topology $\langle \Psi \rangle$, over the range of angular positions from $\theta = 40°$ to 120°, are given in figure 18. These $\langle \Psi \rangle$ patterns clearly show

https://doi.org/10.1017/S0022112010003848 Published online by Cambridge University Press

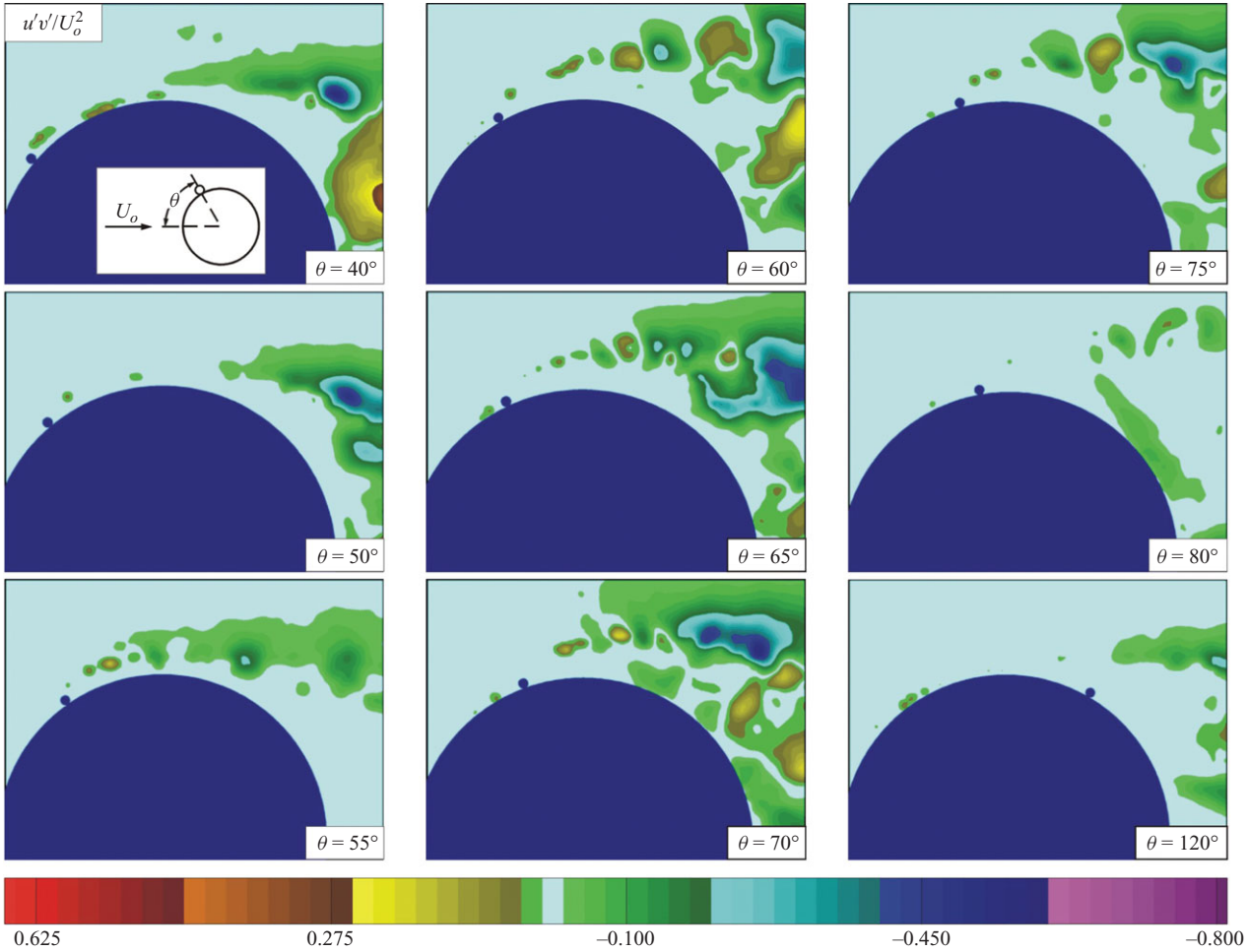

FIGURE 17. Contours of instantaneous Reynolds stress correlation $u'v'/U_o^2$ for angular positions of the wire ranging from $\theta = 40°$ to 120°. Images are selected when the shear layer is at its lowermost position of the transverse fluctuation, directly corresponding to $\omega D/U_o$ patterns, given in figure 16. Minimum and incremental values are as follows: $|[u'v'/U_o^2]|_{min} = 0.025$, $\Delta|[u'v'/U_o^2]| = 0.025$.

https://doi.org/10.1017/S0022112010003848 Published online by Cambridge University Press

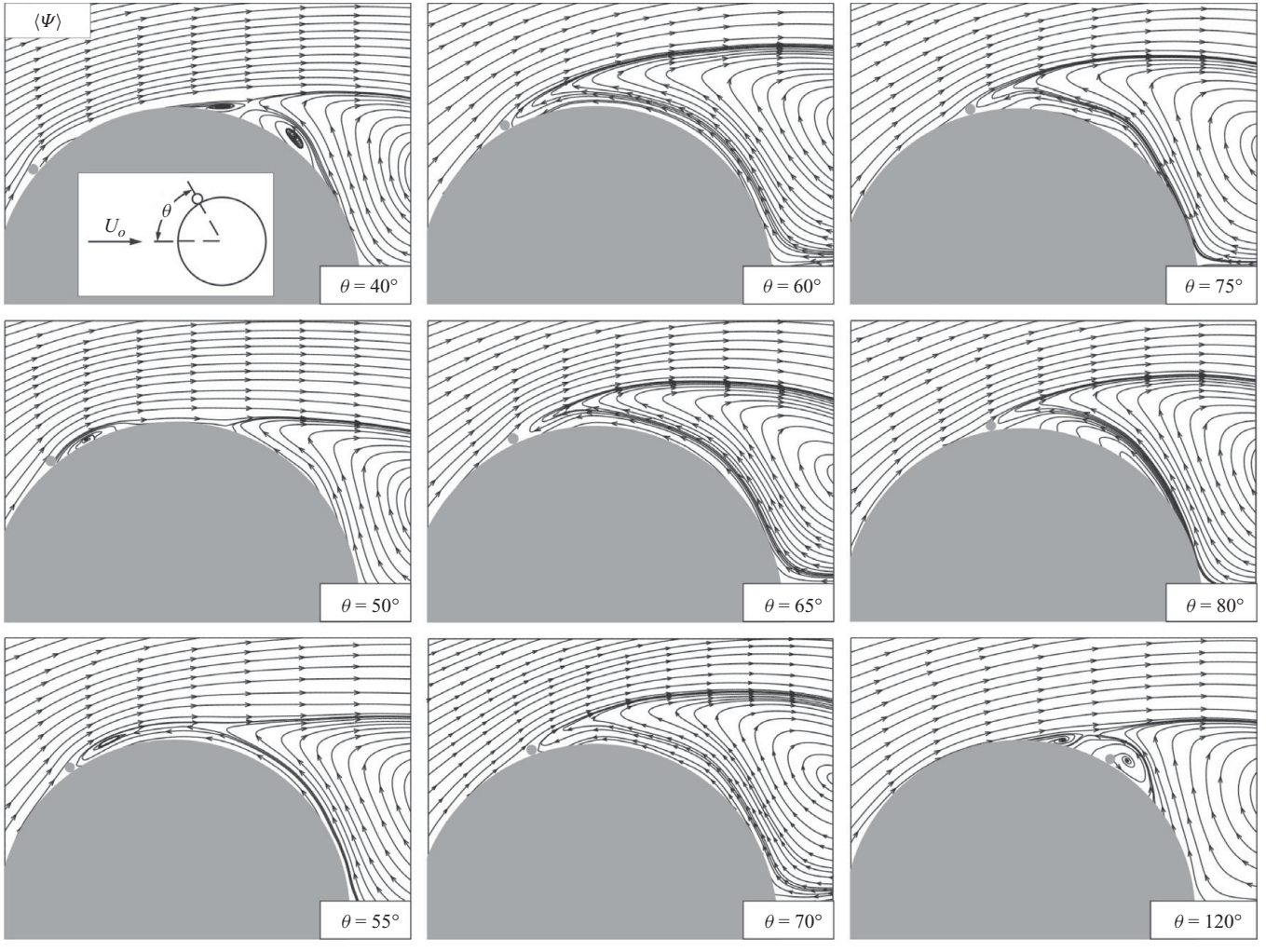

FIGURE 18. Patterns of time-averaged streamline topology $\langle \Psi \rangle$ for different angular positions of the wire ranging from $\theta = 40^\circ$ to 120°.

the behaviour of the separation–reattachment process induced by the wire. At $\theta = 40°$, the shear layer separates at the wire, reattaches and the final separation takes place from the cylinder surface. Immediately downstream of the final separation point, close to the cylinder, so-called 'recirculatory laminar bubbles' form (Singh & Mittal 2005). In the investigation of the effect of increase of Reynolds number on the flow past a smooth cylinder, Singh & Mittal (2005) suggested that upstream movement of small-scale shear-layer vortices can cause the laminar recirculatory bubbles to disappear in subcritical regime. According to figure 16, small-scale vortices advance upstream as θ approaches the second critical angle θ_{c2}. Apparently thereby, laminar bubbles are not observed except at $\theta = 40°$ and 120°. Further observations of the time-averaged streamline topology $\langle \Psi \rangle$ of figure 16 are as follows. At $\theta = 50°$, the shear layer separates at the wire, then reattaches downstream of it, with a relatively long separation bubble compared to that at $\theta = 40°$; eventual separation takes place from the cylinder surface. At the first critical angle $\theta_{c1} = 55°$, flapping of the shear layer between the two stable states, with and without reattachment after the separation at the wire, was shown to be present in the foregoing. Time-averaging of this bistable motion produces a single, horizontal layer of the time-averaged streamline topology $\langle \Psi \rangle$ at $\theta_{c1} = 55°$. This averaged layer can be viewed as the equilibrium position around which the instantaneous shear layer oscillates in a bistable manner. From $\theta = 60°$ to 80°, the shear layer shows complete separation at the wire with no reattachment. A layer of reverse flow is evident; it is drawn from the base region of the cylinder towards the wire, along the cylinder surface. This reverse flow region becomes thicker with increasing θ, and finally at $\theta = 120°$, immediately downstream of the separation, 'recirculatory laminar bubbles' form, resembling the streamline topology at $\theta = 40°$.

5. Concluding remarks

This investigation has focused on alterations of the flow structure around a stationary circular cylinder at $Re = 10\,000$. These alterations are induced by a surface disturbance in the form of a single spanwise wire having a diameter approximately two orders of magnitude smaller than the cylinder diameter. This wire diameter is slightly larger than the local unperturbed boundary-layer thickness at $Re = 10\,000$. Substantial changes are induced in the overall structure of the near wake, the separation/reattachment behaviour of the shear layer, the large-scale Kármán instability, as well as the small-scale shear-layer instability. The principal findings of this study are summarized in the following.

The single wire, mounted spanwise along the surface of the cylinder, perturbs only one of the shear layers, that is, the layer on the wire side of the cylinder, yet the consequences of this local disturbance are found to be global over the entire near wake, provided that the surface wire is located within a certain range of angular positions. It is possible to induce varying degrees of asymmetry of the near wake, and major changes in the time-averaged flow characteristics. Two distinct angles are identified as critical. At one critical angle (designated herein as θ_{c1}), substantial extension, and at the other critical angle (designated as θ_{c2}), significant contraction of the time-averaged near-wake bubble occurs. It has also been shown that the critical states of the near wake, which occur when the surface wire is positioned at these critical angles, are intimately related to substantial changes in the peak values of velocity fluctuation and Reynolds stress.

Global analyses of velocity spectra, based on the time records acquired simultaneously at thousands of locations in the separated shear layers and the

https://doi.org/10.1017/S0022112010003848 Published online by Cambridge University Press

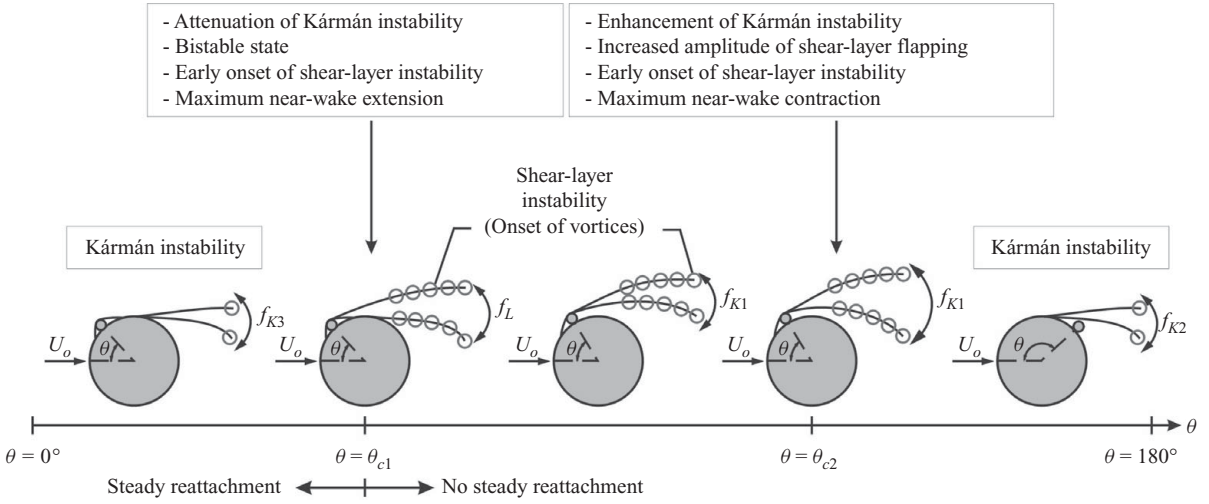

FIGURE 19. Schematic of flow regimes as a function of angular position of the wire. The two critical angular positions of the wire are labelled as θ_{c1} and θ_{c2}. Here, θ_{c1} corresponds to the critical angular position leading to attenuation of Kármán instability, bistable flow regime, early onset of shear-layer instability, and maximum near-wake extension; whereas θ_{c2} is the critical angular position causing enhancement of Kármán instability, increased amplitude of shear-layer flapping, early onset of shear-layer instability, and maximum near-wake contraction. The two extreme positions of the flapping motion are represented via lines; and the small-scale vortices of shear-layer instability via circles. (The size of the wire relative to the size of the cylinder is exaggerated in the schematic for demonstration purposes.)

near wake, have revealed the following phenomena related to the flow instabilities. Significant attenuation of the Kármán instability occurs when the wire is positioned on the surface of the cylinder at the critical angle θ_{c1}, which is associated with the maximum extension of the time-averaged near wake. On the other hand, intensification of the coherence and strength of the Kármán instability occurs when the wire is placed at the critical angle θ_{c2}, which is related to the most significant contraction of the time-averaged near wake. Furthermore, when the spanwise wire is located at the critical angle θ_{c1}, velocity fluctuations in the vicinity and downstream of separation of the shear layer on the wire side have a predominantly broad spectral peak, with a centre frequency that is an order of magnitude lower than the characteristic value of the Kármán frequency. This pronounced low-frequency instability involves bistable oscillations of the shear layer between two distinct separation modes: with and without reattachment downstream of separation at the wire. Finally, the Strouhal number associated with the Kármán instability has been verified to depend on the angular position of the wire within the aforementioned range of angles, where the wire markedly controls the near-wake structure.

The foregoing findings have been related to quantitative images of the onset of the shear-layer instability leading to small-scale vortex formation in the separating shear layer, the associated Reynolds stresses and the spatial extent of the transverse deflections of the shear layer. All of these characteristics are greatly affected by the location of the wire. At the first critical angle θ_{c1}, and at and around the second critical angle θ_{c2} of the wire, the onset of small-scale vortices occurs earlier in the separating shear layer, in comparison to other angular positions of the wire. In particular, in the vicinity of the second critical angle θ_{c2} of the wire, early inception of the shear-layer vortices is accompanied by their early agglomeration, resulting in a significant increase in the instantaneous thickness of the shear layer. Another observation which occurs near the second critical angle θ_{c2} of the wire is relatively enhanced spatial amplitude of the shear-layer flapping.

The schematic of figure 19 summarizes the flow regimes as a function of the angular position of the wire. In this schematic, the two critical angles – θ_{c1} and θ_{c2} – are specifically marked with the distinctive consequences of the wire at these angles. Therein, the circles indicate the onset of the small-scale shear-layer vortices.

The authors are pleased to acknowledge the support of the Office of Naval Research under Grant No. N00014-94-1-0185, monitored by Dr Thomas Swean.

Supplementary movies are available at journals.cambridge.org/flm.

REFERENCES

Aiba, S., Ota, T. & Tsuchida, H. 1979 Heat transfer and flow around a circular cylinder with tripping-wires. *Wärme-Stoffübertrag.* **12**, 221–231.

Alam, M. M., Sakamoto, H. & Moriya, M. 2003 Reduction of fluid forces acting on a single circular cylinder and two circular cylinders by using tripping rods. *J. Fluids Struct.* **18**, 347–366.

Batill, S., Nelson, R. & Nebres, J. 1988 An experimental investigation of the flow field around yawed, stranded cables. *Tech. Rep.* 2201-89-1, contract no. N00014-83K-0239. Naval Coastal Systems Center.

Bourque, C. & Newmann, B. G. 1960 Reattachment of a two-dimensional, incompressible jet to an adjacent flat plate. *Aeronaut. Q.* **11**, 201–232.

Cardell, G. S. 1993 Flow past a circular cylinder with a permeable wake splitter plate. PhD dissertation, Graduate Aeronautical Laboratory, California Institute of Technology, Pasadena, CA.

Chyu, C. K. & Rockwell, D. 2002 Near-wake flow structure of a cylinder with a helical surface perturbation. *J. Fluids Struct.* **16**, 263–269.

Cowdrey, C. F. & Lawes, J. A. 1959. Drag measurements at high Reynolds numbers of a circular cylinder fitted with three helical strakes. *Tech. Rep.* 384. National Physical Laboratory, Teddington, UK.

Dong, S., Karniadakis, G. E., Ekmekci, A. & Rockwell, D. 2006 A combined direct numerical simulation-particle image velocimetry study of the turbulent near wake. *J. Fluid Mech.* **569**, 185–207.

Eaton, J. K. & Johnston, J. P. 1980 A review of research on subsonic turbulent flow reattachment. In *AIAA Thirteenth Plasma and Fluid Dynamics Conference*, Snowmass, CO. *AIAA Paper* 80-1438.

Eaton, J. K. & Johnston, J. P. 1981 Low-frequency unsteadiness of a reattaching turbulent shear layer. In *Third Symposium on Turbulent Shear Flows*, University of California at Davis, Davis, CA.

Ekmekci, A. 2006 Control of the near-wake of a circular cylinder: effects of surface disturbances. PhD dissertation, Department of Mechanical Engineering and Mechanics, Lehigh University, Bethlehem, PA.

Every, M. J., King, R. & Weaver, D. S. 1982 Vortex-induced vibrations of cylinders and cables and their suppression. *Ocean Engng* **9**, 135–157.

Fage, A. & Warsap, J. 1929 The effects of turbulence and surface roughness on the drag of a circular cylinder. *Aero. Res. Comm. R. & M.* No. 1283.

Fox, R. W. & Kline, S. J. 1960 Flow regime data and design methods for curved subsonic diffusers. *Tech. Rep.* PD-6. Department of Mechanical Engineering, Stanford University, Stanford, CA.

Fujita, H., Takahama, H. & Kawai, T. 1985 Effects of tripping wires on heat transfer from a circular cylinder in cross flow (1st report, the pressure distribution around the cylinder and the drag coefficient). *Bull. JSME* **28** (235), 80–87.

Gartshore, I. S., Khanna, J. & Laccinole, S. 1979 The effectiveness of vortex spoilers on a circular cylinder in smooth and turbulent flow. In *Fifth International Conference on Wind Engineering*, Fort Collins, CO.

Hirsch, G., Ruscheweyh, H. & Zutt, H. 1975 Damage on a 140 m high steel stack due to wind-induced transverse vibration (in German). *Der Stahlbau* **2**, 33–41.

Horton, K., Ferrer, C., Watson, K. & Charvoz, D. 1987 Measurements of the hydrodynamic force and strum characteristics of stranded cables. *Tech. Rep.* NCSC TM 471–87. Naval Coastal Systems Center.

Hover, F. S. & Triantafyllou, M. S. 1999 The effects of small wires on vortex-induced vibration parameters for cylinders. *Flow-Induced Vib. ASME* **389**, 97–102.

Hover, F. S. & Triantafyllou, M. S. 2000 Dependence of flow-induced vibration parameters on spanwise trip-wires. In *Flow Induced Vibration* (ed. Ziada & Staubli), pp. 91–96. Balkema.

Hover, F. S., Tvedt, H. & Triantafyllou, M. S. 2001 Vortex-induced vibrations of a cylinder with tripping wires. *J. Fluid Mech.* **448**, 175–195.

Igarashi, T. 1986 Effect of tripping wires on the flow around a circular cylinder normal to an airstream. *Bull. JSME* **29** (255), 2917–2924.

James, D. F. & Truong, Q. S. 1972 Wind load on cylinder with spanwise protrusion. *Proc. ASCE J. Engng Mech. Div.* **98**, 1573–1589.

Lin, J. C., Towfighi, J. & Rockwell, D. 1995 Near-wake of a circular cylinder: control by steady and unsteady surface injection. *J. Fluids Struct.* **9**, 659–669.

Nakagawa, K., Fujino, T., Arita, Y., Ogata, Y. & Masaki, K. 1959 An experimental investigation of aerodynamic instability of circular cylinders at supercritical Reynolds numbers. In *Ninth Japanese Congress of Applied Mechanics*, pp. 235–240.

Nakagawa, K., Fujino, T., Arita, Y. & Shima, K. 1963 An experimental study of aerodynamic devices for reducing wind-induced oscillatory tendencies of stacks. In *Proceedings of the Symposium on Wind Effects on Buildings and Structures.* No. 16, vol. 2, pp. 774–795. Teddington, UK.

Narayanan, R. & Reynolds, A. J. 1968 Pressure fluctuations in reattaching flow. *ASCE J. Hydraul. Div.* **94**, 1383–1398.

Naudascher, E. & Rockwell, D. 2005 *Flow-Induced Vibrations: An Engineering Guide*. Dover.

Nebres, J. V. 1989 Flow around yawed stranded cables. MS thesis, Department of Aerospace and Mechanical Engineering, University of Notre Dame, IN.

Nebres, J. V. 1992 Wake similarity and vortex formation for two-dimensional bluff-bodies. PhD dissertation, Aerospace and Mechanical Engineering Department, University of Notre Dame, IN.

Nebres, J. V. & Batill, S. 1993 Flow about a circular cylinder with a single large-scale surface perturbation. *Exp. Fluids* **15**, 369–379.

Nebres, J. V., Batill, S. & Nelson, R. 1993 Flow about yawed, stranded cables. *Exp. Fluids* **14**, 49–58.

Newman, B. G. 1961 The deflection of plane jets by adjacent boundaries – Coanda effect. In *Boundary Layer and Flow Control, Its Principles and Application* (ed. G. V. Lachman), pp. 232–265. Pergamon.

Nigim, H. H. & Batill, S. M. 1997 Flow about cylinders with surface perturbations. *J. Fluids Struct.* **11**, 893–907.

Nikitina, F. A. & Kulik, A. I. 1980 The interaction of separated flows with periodic external perturbations. *Fluid Mech. – Sov. Res.* **9**, No. 4.

Prasad, A. & Williamson, C. H. K. 1997 The instability of the shear layer separating from a bluff body. *J. Fluid Mech.* **333**, 375–402.

Rockwell D. 1977 Organized fluctuations due to flow past a square cross-section cylinder. *Trans. ASME: J. Fluids Engng* **99**, 511–516.

Ruscheweyh, H. 1981 Straked in-line steel stacks with low mass-damping parameter. *J. Wind Engng Ind. Aerodyn.* **8**, 203–210.

Saelim, N. 2003 Flow past a cylinder: effect of surface modification on structure of the near-wake. PhD dissertation, Department of Mechanical Engineering and Mechanics, Lehigh University, Bethlehem, PA.

Scruton, C. & Walshe, D. E. J. 1957 A means of avoiding wind-excited oscillations of structures with circular or nearly circular cross-section. *Tech. Rep.* 335. National Physical Laboratory, Teddington, UK.

Singh, S. P. & Mittal, S. 2005 Flow past a cylinder: shear layer instability and drag crisis. *Intl J. Numer. Meth. Fluids* **47**, 75–98.

Smith C. R. 1975 A note on diffuser generated flow unsteadiness. *Trans. ASME: J. Fluids Engng* **97**, 377–379.

Smith, C. R. & Kline, S. J. 1974 An experimental investigation of the transitory stall regime in two-dimensional diffusers. *Trans. ASME: J. Fluids Engng* **96**, 11–15.

Votaw, C. W. & Griffin, O. M. 1971 Vortex shedding from smooth cylinders and stranded cables. *Trans. ASME: J. Basic Engng* **93**, 457–460.

Wedding, J. B., Robertson, J. M., Peterka, J. A. & Akins R. E. 1978 Spectral and probability-density nature of square-prism separation-attachment wall pressures. *Trans. ASME: J. Fluids Engng* **100**, 485–492.

Williamson, C. H. K. 1996 Vortex dynamics in the cylinder wake. *Annu. Rev. Fluid. Mech.* **28**, 477–539.

Wong, H. Y. & Kokkalis, A. 1982 A comparative study of three aerodynamic devices for suppressing vortex-induced oscillation. *J. Wind Engng Ind. Aero.* **10**, 21–29.

Woodgate, L. & Mabey, J. F. M. 1959 Further experiments on the use of helical strakes for avoiding wind-excited oscillations of structures of circular or nearly circular section. *Tech. Rep.* No. 381. National Physical Laboratory, Teddington, UK.

Zdravkovich, M. M. 1981 Review and classification of various aero- and hydrodynamic means for suppressing vortex shedding. *J. Wind Engng Ind. Aerodyn.* **7**, 145–189.